ELECTROLYSIS PROPULSION FOR SMALL-SCALE SPACECRAFT

A Dissertation

Presented to the Faculty of the Graduate School

of Cornell University

In Partial Fulfillment of the Requirements for the Degree of

Doctor of Philosophy

by

Rodrigo A. Zeledon

May 2015

ELECTROLYSIS PROPULSION FOR SMALL-SCALE SPACECRAFT

Rodrigo A. Zeledon, Ph. D.

Cornell University 2015

In the past decade, CubeSats have revolutionized small spacecraft missions. These miniature satellites began as educational projects but have lowered the bar for access to space and enabled research institutions and companies to launch technology demonstration and science missions in low Earth orbit. Propulsion systems small enough to fit in a CubeSat can extend the benefits of CubeSats beyond low Earth orbit, and potentially even allow for small-scale interplanetary missions. Propulsion systems designed for CubeSats must overcome severe restrictions in their chemistry, dimensions, mass and operation scheme for the sake of fitting within the CubeSat deployer and conforming to CubeSat specifications.

This research presents a novel concept for small satellite propulsion based on the electrolysis of water. These systems are designed to ensure the safety of the launch vehicle and overcome the restrictions imposed by operating as a secondary payload by avoiding the use of hazardous materials, pressure vessels and explosives. Numerical analyses are used to predict the performance of the propulsion system. Vacuum chamber experiments on a prototype of the propulsion system are conducted to determine the performance of the system.

An analysis of the attitude dynamics and operation of a satellite with an electrolysis propulsion system are presented. The propulsion system as well as the attitude control of the spacecraft are aided by the spacecraft's spin about its major axis

of inertia. Energy damped by the water carried on board keeps the satellite stable and damps nutation caused by external torques and the use of the propulsion system.

Several applications are presented for low earth orbit as well as interplanetary CubeSats. The design of a mission to navigate a CubeSat to lunar orbit as part of NASA's CubeQuest Challenge is detailed. Prospects for broader applications of this work involving distributed exploration using in-situ water are identified.

BIOGRAPHICAL SKETCH

Rodrigo Zeledon grew up in San José, Costa Rica and completed his high school education at Country Day School in Escazú in 2005. He then attended the Massachusetts Institute of Technology where he obtained the degree of Bachelor of Science in Aerospace Engineering in June of 2009. He moved to Ithaca, NY in 2009 to pursue his graduate studies at Cornell. There he joined Dr. Mason Peck's Space Systems Design Studio, initially working on steering laws for control moment gyroscopes before focusing on electrolysis propulsion systems.

Para mi familia, que me ha apoyado en las buenas y en las malas todos estos años.

ACKNOWLEDGMENTS

I would like to thank my advisor, Dr. Mason Peck, for all his help and guidance. Mason, your advice and enthusiasm for my work have been a continued source of motivation. Your passion for your work and for the field has been a great example in my graduate studies. I would also like to thank the members of my committee, Dr. Mark Campbell and Dr. Peter Gierasch, for their guidance and perspective. I would like to specifically mention Dr. Ephrahim Garcia, who was the fourth member of my committee, for his help and advice during the most difficult parts of my time at Cornell, and for his encouragement in the form of repeated shouts of "why haven't you graduated already?"

I would like to thank my parents and grandparents, who early on cultivated in me a sense of curiosity and of the importance of being ethical. They have always been there for me when I needed advice, encouragement, a fresh perspective, or simply a rum and coke. Their love and support have been constant throughout my life, and for that I cannot thank them enough. My sister, Mariela, has always been an inspiration and a role model. Beginning in grade school, she has always set an extremely high bar for me.

I would like to give thanks to the alumni, staff and current students of the Space Systems Design Studio. Laura, thanks for the encouragement and help as we toiled on CMG papers, and for all your help in the job search! Justin, Joe, and Mike, thanks for setting a great example. Liran, Zac, Ben, and Lorraine, thanks for the insightful chats, discussions and help throughout these years. Ryan, other Ryan, Kyle, Frankie and Hunter, best of luck in the journey ahead, you guys are a great team!

To the MAE staff, especially Marcia and Patti, thanks for being a beacon in the bureaucratic fog that Cornell can sometimes be. Your ability to keep things running

smoothly amazes all of us.

To all of the undergraduate and M.Eng students who worked on my project, I cannot thank you enough. Your hard work has been absolutely crucial to the project, and I'm extremely thankful for having the opportunity to work with such talented people.

To the amazing friends I made in Ithaca, and to old friends who have encouraged me throughout these years, I really could not have made it without you. I will miss all of the fun times in Ithaca, and look forward to hearing about the amazing things you are all doing.

Finally, I would like to thank the organizations that have provided funding for me and for my project. Without their generous support, none of this would have been possible. I would like to thank the Alfred P. Sloan foundation, the National Action Council for Minorities in Engineering and Cornell Diversity Programs in Engineering for awarding me a Sloan grant. I would also like to thank Moog, Inc. for providing funding, advice and engineering support for the project, as well as Northrop Grumman, New York NASA Space Grant, and NASA/JPL for their support.

TABLE OF CONTENTS

LIST OF FIGURES

Appendix

LIST OF ABBREVIATIONS

P-POD	Poly-PicoSatellite Orbital Deployer
U	CubeSat Unit, approximately a 10 cm x 10 cm x 10 cm volume
LEO	Low Earth Orbit
ACS	Attitude Control System
GEO	Geostationary Earth Orbit
GTO	Geostationary Transfer Orbit
NASA	National Aeronautics and Space Administration
SLS	Space Launch System
EM-1	Exploration Mission 1
AU	Astronomical Unit
PEM	Polymer Electrolyte Membrane
STP	Standard Temperature and Pressure
CM	Center of Mass
CAD	Computer Aided Design
PD	Proportional-Derivative control
IGRF	International Geomagnetic Reference Field
TLE	Two-Line Element
NORAD	North American Aerospace Defense Command
GPS	Global Positioning System
CMOS	Complementary metal–oxide–semiconductor
RAM	Random-Access Memory

LIST OF SYMBOLS

ΔV	change in orbital velocity, m/s
n_{H2}	moles of hydrogen gas, mol
P_{elec}	electrical power, W
t	time, s
η	electrolyzer efficiency
H_f	heat of formation, J/mol
V_{tank}	total tank volume, m^3
p	pressure, Pa
R	universal gas constant, J/(mol K)
T	temperature, K
V_{gas}	volume of electrolyzed gas, m^3
γ	specific heat ratio
M	molar mass, kg/mol
v	fluid velocity, m/s
A	cross-sectional area, m^2
F	thrust, N
$\dot{m}$	mass flow rate of propellant, kg/s
g_0	acceleration due to gravity at the earth's surface, m/s^2
I_{sp}	specific impulse, s
Δm	change in mass, kg
I	impulse, N s
m_{prop}	propellant mass, kg
m_{sat}	satellite mass, kg
Bo	Bond number
$\Delta\rho$	density difference, kg/m^3
a	acceleration, m/s^2
σ	surface tension, N/m
L	characteristic length, m
$\boldsymbol{\omega}$	spacecraft angular velocity, rad/s
$\boldsymbol{r}$	distance between fluid's free surface and spacecraft center of mass, m
$\boldsymbol{I}$	spacecraft inertia dyadic, kg m^2
$\boldsymbol{H}$	spacecraft angular momentum vector, Nms
$\boldsymbol{\tau}$	torque acting on spacecraft, Nm
θ	precession angle, rad
$\boldsymbol{\tau}_M$	torque produced by magnetorquers, Nm
$\boldsymbol{M}$	magnetic moment, Am^2
$\boldsymbol{B}$	magnetic field, T
R_E	Earth radius, m
B_0	magnitude of Earth's magnetic field, T
φ	total reorientation angle, rad
$\boldsymbol{\tau}_{GG}$	gravity gradient torque, Nm

μ	Earth geopotential, m^3/s^2
$\boldsymbol{\tau}_{GG}$	gravity gradient torque, Nm
$\boldsymbol{r}_{sat}$	position of spacecraft center of mass relative to Earth's center, m
ν	true anomaly, rad
$\boldsymbol{\tau}_S$	torque due to solar pressure, Nm
F_{SC}	solar illumination constant, W/m^2
c	speed of light, m/s
C_A	absorption coefficient
A	illuminated cross-sectional area, m^2
d	solar torque moment arm, m
$\hat{\boldsymbol{s}}$	sun direction vector
$\hat{\boldsymbol{n}}$	surface normal vector
$\hat{\boldsymbol{x}}, \hat{\boldsymbol{y}}, \hat{\boldsymbol{z}}$	spacecraft body normal vectors

CHAPTER 1

INTRODUCTION

Propulsion systems for CubeSats have been of interest to the CubeSat community ever since the inception of the CubeSat standard [1]. As the development of other technologies critical to the use of CubeSats in interplanetary missions has progressed, technology development for propulsion systems has taken on even greater urgency [2]. The deployment methods used for CubeSats today include deployment as secondary payloads or deployment from the International Space Station. Both of these methods, however, impose strict limitations to candidate propulsion systems at this scale [3]. The technology challenge is not merely the reduction of existing large-scale propulsion into an envelope small enough to fit in one of these satellites. Rather, the main limitations have to do with safety, both for the primary payload and for those tasked with handling and integrating the CubeSat onto the rocket [4]. Most large-scale propulsion schemes make use of explosive and reactive chemicals, materials stored either cryogenically or at high pressures, or propellants that are toxic and require special handling. While a technology-demonstration system employing one of these schemes could fly on a CubeSat provided the proper waivers are obtained, the risk and paperwork involved make it unlikely that such a propulsion system could gain acceptance as a system to be used regularly on many CubeSat missions.

Large-scale electrolysis propulsion systems were first proposed by Stechman and Campbell in 1973 as a means of providing primary propulsion and attitude control for large satellites [5]. These concepts were advanced by Stedman in 1976 by

introducing the regenerative fuel cell [6]. The regenerative fuel cell made it possible to use the system as a battery since it provides energy storage in the form of chemical energy [7]. The process can then be reversed to provide electric power when needed [8]. This system could also be used to provide drinking water and oxygen to the crew, albeit at the expense of the storage and propulsive capabilities of the system [9]. The operational flexibility of the system came at the expense of storage volume and mass. In order to use the fuel cells to generate electricity, the hydrogen and oxygen gases need to be separated during the electrolysis process and then stored in separate tanks [10]. This scheme makes the system bulky and complex, which prevented its acceptance on flight programs. These large-scale concepts were revisited in the 1990's by de Groot et. al. and their merits as integrated power and propulsion modules for small spacecraft were also examined [11] [12]. However, the complexity of the regenerative system limits its applications.

CubeSats have existed since 2000 [13] and in the past decade and a half have transformed from educational projects to tools for much broader research and technology demonstration missions. Conforming to CubeSat standards has two main benefits [14]. First, it allows for ready integration with the launch vehicle by specifying agreed-to dimensions and mass properties of the CubeSats. The launch vehicle only needs to incorporate a standard deployer, either the P-POD or its 6U version [15], inside of which any CubeSat that adheres to the standards can be integrated. Second, the standardized sizes allow for the use of off-the-shelf components. This feature permits the CubeSat designer to focus on the payload or on the experimental components, reducing the cost and time necessary to develop custom

components for every subsystem. In these two ways, CubeSats lower the bar for access to space by reducing the cost and complexity associated with larger spacecraft.

So far, all CubeSats have operated in low Earth orbits determined by the deployment from the launch vehicle. However, none have incorporated propulsion capable of substantial ΔV. In order to extend the operational envelope of CubeSats beyond Low Earth Orbit (LEO), or to provide CubeSats with a means of significantly changing their orbits, a propulsion system beyond the current state of the art is required. Such a propulsion system should also be consistent with the general philosophy of CubeSats, providing the required performance at a low cost and under strict power, mass and volume limitations.

The development of a propulsion system for CubeSats (or other secondary payloads) involves accommodating restrictions not only in mass and volume, but also restrictions in the use of hazardous propellants, launch-vehicle safety, use of pressure vessels, power consumption, and cost, to name a few. Electrolysis propulsion systems fit well within these constraints and represent a viable option for high ΔV propulsion at the CubeSat scale. An electrolysis propulsion system uses only water as propellant, is unpressurized and safe during launch, can operate in very low power modes, and leads to a relatively inexpensive system.

This dissertation highlights several contributions made in the field of small spacecraft propulsion systems and dynamics. The concept and architecture for an electrolysis propulsion system for small spacecraft is presented. The test equipment and experimental setup required for testing the performance of the system is described and results from early performance tests are presented.

Demonstration missions are an important part of technology development. Another contribution, with the aim of supporting a future demonstration mission, is the evaluation of system architectures for two possible demonstration missions. These case studies highlight the utility of electrolysis propulsion systems in missions beyond LEO, and missions where impulsive ΔV is desired.

The final contribution is the use of the satellite's passive dynamics to simplify the design of the propulsion system and reduce the number of required attitude control system (ACS) actuators. The energy dissipation from the fluid slosh in the water tank contributes to restoring a major axis spin, which is the lowest energy state for the spacecraft. This fact allows for a design of an attitude control system that requires only a single cold gas thruster to control the direction, but not the magnitude, of the angular momentum. This in turn means that the direction about which the spacecraft is spinning can be controlled, but the phase of the spin or the spin rate cannot be controlled by the cold gas thruster. This control system vastly reduces the number of required actuators, and as an added benefit, the satellite spin also provides passive gyroscopic stiffness in the presence of external torques.

The architecture proposed here takes advantage of the small size and limited mass of the 3U CubeSat bus to motivate the design of a propulsion system that, while similar in the fundamental operation to large electrolysis systems, affords several key benefits that make it especially suitable at the CubeSat scale or for use on secondary payloads. These benefits could allow electrolysis propulsion systems to operate safely as secondary payloads and provide primary propulsion for CubeSats in Low Earth

Orbit, or even interplanetary CubeSats on their way to the moon, asteroids and beyond.

The system works by converting solar energy into chemical energy, which can be used to propel the spacecraft. The electricity generated by the solar cells is used to electrolyze liquid water into hydrogen and oxygen gas. Effectively, the propellant itself serves as a battery, storing the electrical power with far greater mass efficiency and none of the electrical losses associated with batteries. The mass savings due to eliminating batteries for the propulsion system and replacing that mass with propellant is a striking benefit of this architecture. Each of the electrolyzers operates at 2V and uses 2W of power. Several electrolyzers are used in parallel, so that the number of electrolyzers that are operational at any point determines the power devoted to electrolysis. This allows the propulsion system to be flexible in its power use, accommodating other subsystems or payloads that might also require some of the limited power available on the CubeSat. This design can potentially eliminate the need for deployable solar panels that are a requirement for many other electric propulsion options at the CubeSat scale.

The tank pressure rises as water is electrolyzed into hydrogen and oxygen. This gas is kept as a mixture, not separated into hydrogen and oxygen tanks. When the gas pressure is sufficiently high and a burn is desired, a solenoid valve opens to allow gas to flow into a combustion chamber. The flight computer then activates a miniature spark plug that ignites the gas mixture. The combustion products then expand through a small nozzle located near the spin axis, generating thrust.

The spacecraft spins in order to separate the water from the oxygen and hydrogen mixture in the fuel tank, ensuring that the valve leading to the combustion chamber always ingests gas, not water. This spin axis is designed to lie as close as possible to the thrust axis. The spin is established after spacecraft separation from the CubeSat deployer. This spin can be achieved by magnetic torquers embedded in the solar panels or by deploying a reaction mass. The spin rate must be high enough to both effectively separate the water from the electrolyzed gases and provide gyroscopic stability in the presence of disturbance torques. Therefore, the spacecraft cannot actuate the spin via reaction wheels, as this would lead to a non-stiff, zero-momentum spacecraft. The attitude dynamics of the spacecraft, including simplified reorientation schemes made possible by the use of a spinning satellite, is one of the focus areas of this work.

Possible applications of this technology include Low Earth Orbit lifetime extension, orbit change maneuvers, and main propulsion for interplanetary missions. A concept for such a mission is analyzed, beginning with deployment on a lunar insertion orbit or lunar flyby. This mission is designed to be compatible with NASA's CubeQuest centennial challenge, which would include a 6U slot on the first launch of the Space Launch System (SLS), EM-1. This concept may also have broader impacts, particularly in the use of *in-situ* water to extend the use of the propulsion system to Earth return without the need to transport propellant from Earth. These prospects are identified but left for future work.

CHAPTER 2

DESIGN AND TESTING OF ELECTROLYSIS PROPULSION SYSTEMS

Basic Operation

The electrolysis propulsion system is composed of a liquid water tank with embedded electrolyzers, a combustion chamber and a nozzle. At launch, the liquid water tank is at atmospheric pressure and therefore the system is inert. The electrolyzers are powered by electricity from solar panels, supplied through the satellite's power distribution system. Several arrangements of valves are possible downstream of the liquid water tank. In the baseline architecture, the water tank is isolated from the combustion chamber by a solenoid valve, which is normally closed and can be opened through a signal from the flight computer, and a passive check valve. A second check valve between the combustion chamber and the nozzle prevents any gas from escaping before the explosion. The second arrangement of valves sacrifices some performance and simplifies the operation by removing the check valve between the combustion chamber and nozzle. The third arrangement involves only passive check valves. This arrangement requires careful selection of the cracking pressures, but would not require any actively-controlled valves.

In any of these three arrangements the amount of gas generated cannot sustain continuous combustion and propulsion. The combustion chamber contains a miniature spark plug, which ignites the gas in a controlled explosion in the combustion chamber. The general operating scheme is shown in Figure 1, and the two alternate valve arrangements are shown in Figure 2.

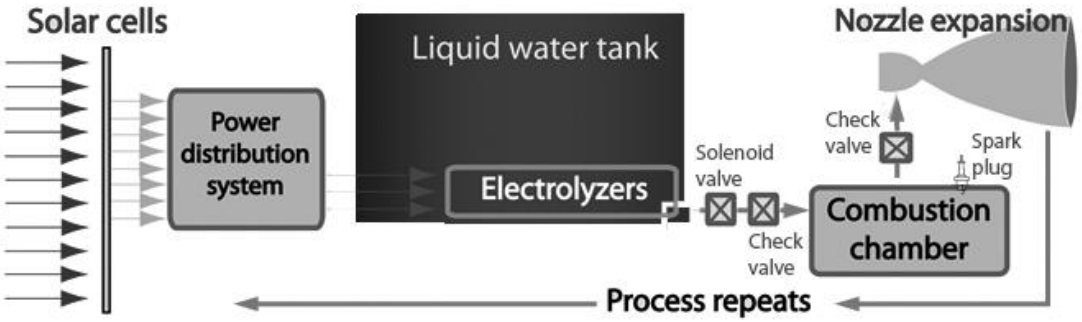

Figure 1. Schematic of the operation of an electrolysis propulsion system.

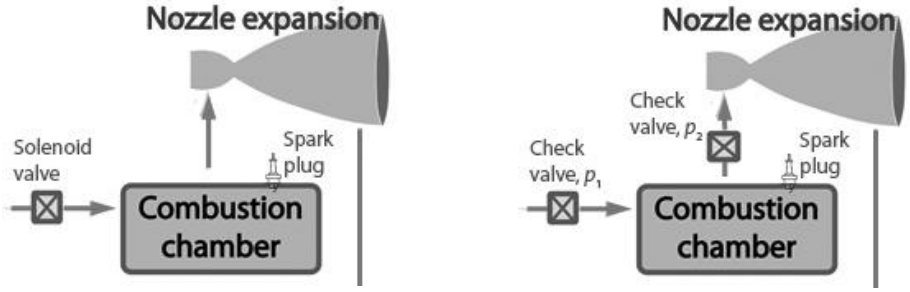

Figure 2. Two alternate valve arrangements downstream of the water tank.

A. Electrolysis

The first step in the operation of the propulsion system is the electrolysis of the liquid water. The distilled water is broken down into gaseous hydrogen and oxygen by electrolyzers which are mounted on the inside of the water tank. Other electrolysis

concepts, including those proposed for large spacecraft and primary launch vehicles, store the gases separately in two tanks. These larger systems include dryers and various mechanisms and pumps to ensure that no cross contamination occurs. The propulsion systems then use the separate gases stored at high pressure or as liquids in a conventional injector-type combustion chamber [5]. The electrolysis propulsion system for CubeSats operates with pre-mixed hydrogen and oxygen as a single gas—a stoichiometric ratio of H_2 and O_2—and therefore the gases are stored together in the liquid water tank. This architecture reduces the complexity, mass and size of the system at the expense of not being able to use the stored hydrogen and oxygen to generate electricity through a regenerative fuel cell.

The energy required to separate the liquid water into hydrogen and oxygen gas is the heat of formation of water multiplied by the efficiency of the electrolyzer, along with some minor losses. The heat of formation here is the energy required to break down one mole of water into one mole of hydrogen gas and half a mole of oxygen gas. For every gram of water electrolyzed, the spacecraft must generate at least 15.86 kJ, which at a power of 6 W would take the spacecraft 0.73 hours. The amount of hydrogen produced is given by dividing the energy supplied to the electrolyzers by the heat of formation, then multiplying by η, the efficiency of the electrolyzers in converting electrical energy into chemical energy:

$$n_{H2} = \frac{P_{elec} t \eta}{H_f} \quad (1)$$

A typical 3U spacecraft at 1 AU from the Sun can generate anywhere between 2 and 10 W using only body-mounted solar panels, depending on its orientation. The

power profile for a 3U spacecraft in a Geostationary Transfer Orbit (GTO) is shown in Figure 3. The 3U spacecraft contains three electrolyzers, each operating at 2W. This allows the system to operate at 2, 4 or 6W, depending on the available power, spacecraft operating mode and power consumption of other subsystems. As these electrolyzers break down the water into H_2 and O_2 gas, the pressure in the chamber increases. In the case of the design tested as part of this work, the initial pressure in the tank before the electrolysis process begins is 1 atm, which could be established prior to sealing the tank with either hydrogen, oxygen, air, or a mixture of hydrogen and oxygen. If we make the likely assumption that a stoichiometric mixture of hydrogen and oxygen results from the electrolysis, the entire volume of gas after electrolyzing will be hydrogen and oxygen in a stoichiometric ratio, and the fractions will not vary with the cycle number. The total volume of the tank (V_{tank}) is approximately 0.8 L for the 3U spacecraft studied in depth here. The volume of gas before operation, and therefore the initial fill fraction, is a parameter to be chosen based on the mission's required ΔV profile. The electrolyzers generate gas at a rate that is dependent on the power used and the efficiency of the electrolyzers.

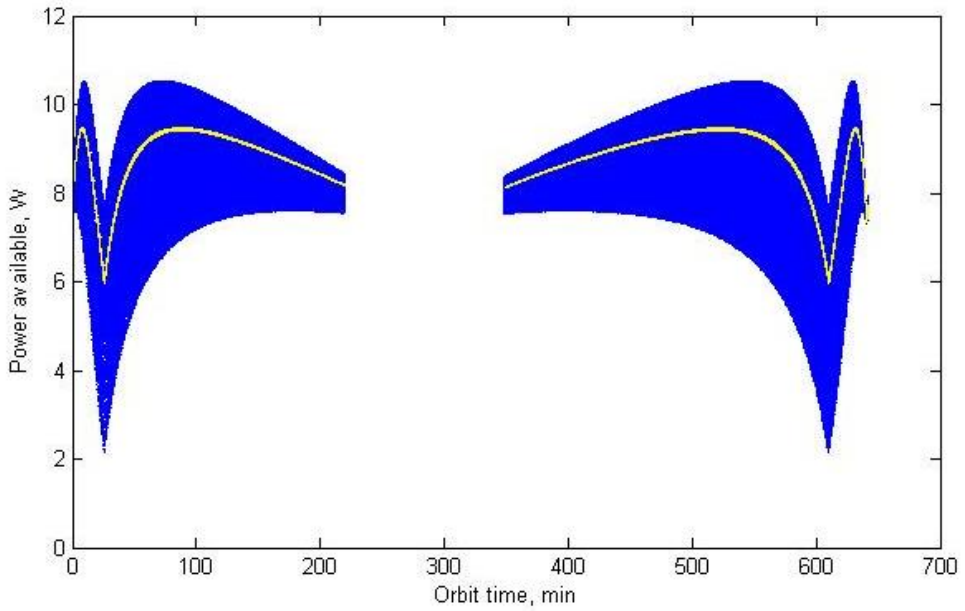

Figure 3. Electrical power available to a CubeSat in an example GTO orbit. *The blue line shows the power for a rotating 3U CubeSat using body-mounted solar panels. The yellow line shows the power averaged to remove the effects of spacecraft rotation.*

Since the electrolysis reaction produces one mole of H_2 and half a mole of O_2 for every mole of H_2O, the number of moles of gas produced by the reaction is $\frac{3}{2}n_{H2}$ for every mole of H_2O. From the ideal gas law, the pressure inside the tank is

$$p = \frac{3P_{elec}t\eta RT}{2H_f V_{gas}} \quad (2)$$

If the initial ullage volume is very small, then V_{gas} is proportionately small at the beginning of the mission. Therefore, the pressure increases very rapidly when the electrolyzers are powered, but only a small mass of water will have been electrolyzed. Therefore, the pressure in the tank decreases significantly after a firing, and the system can fire only a few times before it must electrolyze to build up the pressure. If the initial ullage volume is large, the system takes a longer time to recharge but can

provide more ΔV at the beginning of the mission. For missions that require a quick burst of ΔV at the start, this ullage can be a benefit. The ability to provide larger ΔV at the beginning of the mission, however, comes at the expense of the total mission ΔV because the tank begins at a lower fill fraction.

The efficiency of the electrolyzers can be characterized by measuring the power into the electrolyzers and the amount of gas generated. Rearranging Equation 2 to solve for the efficiency,

$$\eta = \frac{n_{H2} H_f}{P_{elec} t} \quad (3)$$

The numerator of Equation 3 can be determined via the ideal gas law by measuring the volume and pressure of the gas generated in time *t* at a controlled temperature *T*. Equation 3 then becomes

$$\eta = \frac{pVH_f}{RTP_{elec} t} \quad (4)$$

The electrolyzers were tested to determine their efficiency and compared against alkaline electrolyzers operating with potassium hydroxide solutions. The KOH electrolyzers have maximum efficiencies of 72% +/- 4%. The PEM electrolyzers have a greater efficiency, measured to be 92% +/- 4% [16].

B. Combustion

Once the pressure in the tank is high enough for a firing, the flight computer activates the solenoid valve downstream of the water tank. Because of the satellite's rotation, only gas is ingested into the manifold that connects the tank to the combustion chamber [17]. The pressure of the gas needs to be high enough to open the

check valve that is downstream of the solenoid valve. This valve serves to protect the solenoid valve from the explosions that happen in the combustion chamber, and can have a very low cracking pressure, usually on the order of a few psi. Typical off-the-shelf check valves for this application can withstand a back pressure up to 5000 psi, whereas the commercially-available solenoid vales that are small enough for the system typically have maximum pressures of at most 1000 psi. The functionality of the check valve and solenoid valve could be condensed into a single solenoid valve that can withstand back pressures above the combustion pressure, but these valves are either too large or not commercially-available. While the operating pressure can be chosen to some extent, the combustion and expansion processes are more efficient at higher pressures.

The solenoid valve needs to open long enough that the pressure reaches equilibrium in the combustion chamber. In practice this happens within 0.5 s of the valve opening for operating pressures approximately 50 psi to 100 psi. The valve is

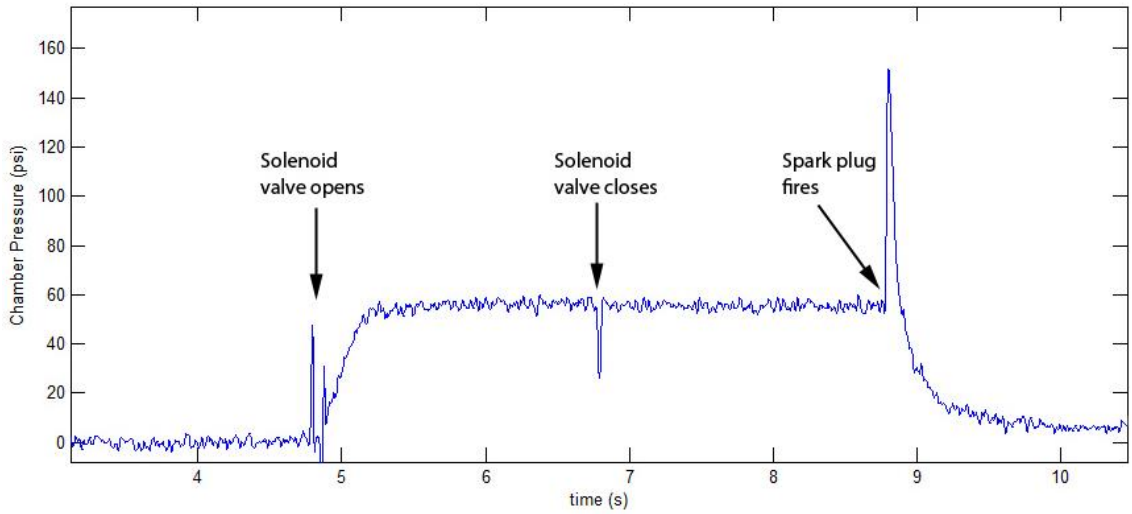

Figure 4. Pressure in the combustion chamber during a test firing.

then closed to conserve power. The gas is kept from escaping the combustion chamber by the second check valve. This valve is downstream of the combustion chamber, before the nozzle. The cracking pressure of this valve needs to be greater than the difference between the operating pressure of the water tank and the cracking pressure of the first check valve. While some margin should be used, a cracking pressure that is too high sacrifices performance. This sequence of events is shown in Figure 4 for a test firing in the vacuum chamber.

Once the solenoid valve is closed, the chamber is armed for firing. This firing does not need to take place immediately, but enough margin should be allowed for the valves to close completely. Combustion is initiated only when enough activation energy is applied to the hydrogen/oxygen mixture [18]. This energy comes from a spark plug embedded in the chamber. The spark plug is also an off-the-shelf part and is powered by a 5V line through a simple capacitive charging circuit. The command to activate the spark plug comes from the flight computer as well.

Combustion in the chamber increases the pressure and temperature of the gas enough that the check valve between the chamber and nozzle is opened. The laminar speed of the flame at the operating temperature and pressure is approximately 20 m/s [19] so the flame should propagate through the chamber in at most 2.4 ms, or about 1% of the duration of a pulse. The gas is then expanded by the nozzle, generating thrust. Because the mixture of hydrogen and oxygen is stoichiometric, the resulting product of combustion is almost exclusively steam.

C. Theoretical performance

A numerical model to estimate the performance of the engine was implemented in MATLAB. This model was then also implemented in ANSYS/Fluent in order to verify the performance characteristics. Combustion is assumed to occur at a much faster scale than the speed of sound and therefore faster than the fluid flows out of the nozzle. For this reason, the gas can be assumed to combust in a fixed volume. The temperature of the gas after combustion is therefore given by the change in enthalpy of the gas, and the pressure is given by the ideal gas law [20].

$$\int_{T_0}^{T_f} C_p(T)dT = \sum_p n_p h_p(T_f) - \sum_r n_r h_r(T_0) \quad (5)$$

The reactants in Equation 5 above are the hydrogen and oxygen gas, which are assumed to be at STP, while the products are assumed to be mainly water vapor at the final combustion temperature. This gas is then expanded to vacuum through a parabolic nozzle. The conditions at the chamber are taken to be the stagnation conditions and the flow is assumed to be isentropic, such that the following relation holds

$$T_x/T_x = \left(p_x/p_y\right)^{(\gamma-1)/\gamma} \quad (6)$$

The velocity at any axial position along the nozzle is a function of the pressure at that position and the stagnation temperature, and is given by [21]

$$v_x = \sqrt{\frac{2\gamma}{\gamma-1}\frac{RT_1}{M}\left[1-\left(\frac{p_x}{p_1}\right)^{(\gamma-1)/\gamma}\right]} \quad (7)$$

The pressure at any axial position along the nozzle is in turn a function of the area ratio, and is given by [21]

$$\frac{A_t}{A_x} = \left(\frac{\gamma+1}{2}\right)^{\frac{1}{\gamma-1}} \left(\frac{p_x}{p_1}\right)^{1/\gamma} \sqrt{\frac{\gamma+1}{\gamma-1}\left[1-\left(\frac{p_x}{p_1}\right)^{(\gamma-1)/\gamma}\right]} \qquad (8)$$

These equations can be solved numerically in an iterative approach that takes into account the varying initial conditions in the throat and the temperature dependence of the specific heat ratio. This analysis results in an average velocity at the nozzle exit of 3068 m/s. This exit velocity implies a specific impulse of 313 s. In practice, the specific impulse can be expected to be comparable but somewhat lower because of losses in the check valve, surface roughness in the nozzle and heat loss through conduction to the walls.

A similar analysis using ANSYS/Fluent provides an estimate of average specific impulse of 366 s. This model uses the initial conditions generated by the MATLAB model as quasi-static time-varying boundary conditions The velocity profile for this simulation is shown in Figure 5.

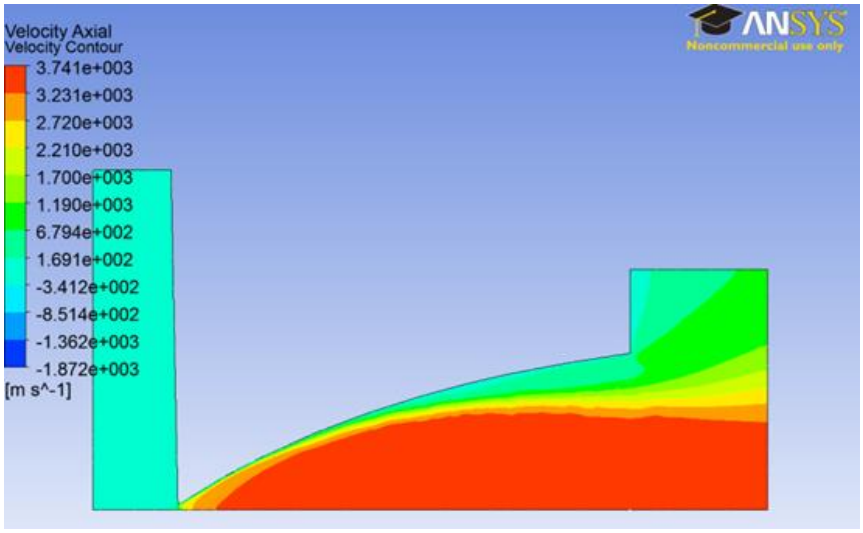

Figure 5. ANSYS/Fluent simulation of fluid flow through the nozzle.

Alternative configurations

The baseline configuration involves an actuated valve and two passive check valves. However, several other valve arrangements are also possible that can offer simplified performance at the expense of specific impulse or thrust.

Simplified operation can be achieved by foregoing the check valve between the combustion chamber and the nozzle. This valve prevents gas from escaping before the spark plug is fired, but with a small enough throat diameter, the amount of gas that escapes is small. The nozzle and chamber could be constructed as a single piece. The diameter of the throat becomes a parameter that balances what is necessary for an optimal nozzle expansion and the rate of escape of the gas before the spark plug is fired. When the solenoid valve is opened, the pressure in the combustion chamber increases until the solenoid is closed. At that point, pressure decreases. Ideally, the spark plug would ignite the gas immediately after the solenoid closes, but in practice a

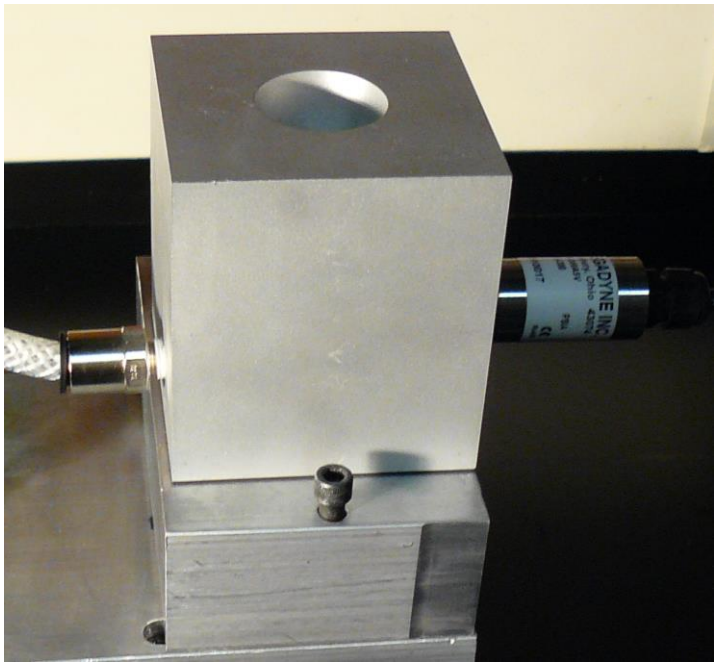

Figure 6. Prototype with combustion chamber and nozzle as a single block.

small amount of time is needed so that the valve can fully close. This timing can be optimized in order to maximize the pressure, and therefore the thrust, generated by the engine.

The second alternative scheme is a system that uses only passive check valves, therefore reducing the complexity of the system. The only controls of the system would be the power to the electrolyzers and the spark plug. Because there is no actuated valve, the system must include a check valve before the nozzle to prevent the gases from escaping. The cracking pressure of these check valves must be carefully selected so that the system operates at the required pressure. The check valve between the water tank and the combustion chamber is set at a cracking pressure p_1. The check valve between the combustion chamber and the nozzle is set at a cracking pressure p_2. p_2 should be slightly larger than p_1, so that no gas escapes before the mixture is ignited. If the cracking pressure p_2 is much larger than p_1, the valve causes a large drop in pressure and the engine's efficiency decreases.

This second configuration can also include a method of recapturing water vapor after each firing and delivering it back to the water tank. Otherwise, a significant amount of water vapor in the combustion chamber can hinder the ignition of the hydrogen/oxygen mixture. The recapture of water vapor can be accomplished via absorbent walls, or thin capillaries in the combustion chamber that allow water to flow back into the tank. A method of recapturing water has not yet been designed and would be required before this scheme can be tested or implemented.

Performance tests

The goal of performance tests is to attain values of specific impulse, thrust and chamber pressure that can be used to analyze the system, optimize it, and provide performance parameters for implementation in missions. These tests are necessary before a final flight version of the propulsion system can be designed, as the size and mass of many of the components depends on the values attained during testing.

A. Equipment

The prototype system developed at Cornell University's Space Systems Design Studio has approximately the same internal dimensions that a 3U flight version would have, and it is designed for testing inside a vacuum chamber. Operation in Earth's gravity simplifies the operation of the thruster because there is no need to spin the propulsion system to provide the acceleration field that achieves gas separation. Instead, the tank is mounted at a right angle from the thruster, in order for the gas to rise to the top of the tank. The thruster points up so that the force can be measured by load cells below the prototype. Dynamical testing of a mass mockup to verify the spin-actuated gas separation and the effect of fuel slosh will be done independently of the initial prototype propulsion system.

The components of the brassboard prototype are analogous to the components of the flight version described in the *Basic Operation* section. A single tank stores the liquid water propellant and electrolyzed gases. Three electrolyzers are installed inside the tank. Electrical power is supplied to the electrolyzers from an external power supply, through a feedthrough installed in the tank. A pressure transducer monitors the

internal pressure of the tank to indicate when the pressure is high enough for a firing to occur.

Gas is allowed to flow into the combustion chamber when the pressure is sufficiently high, above 0.7 MPa for the test prototype. A solenoid valve controls the flow of gas into the combustion chamber. Gas is prevented from escaping the combustion chamber by a check valve between the chamber and the nozzle. A miniature spark plug ignites the hydrogen and oxygen mixture inside the combustion chamber once the signal for firing is given by the flight computer. A microcontroller sets the timing of the solenoid valve and the firing of the spark plug. The nozzle has the same internal dimensions as a flight nozzle but with thicker walls in order to provide a more rigid attachment with the combustion chamber. Figure 7 shows a

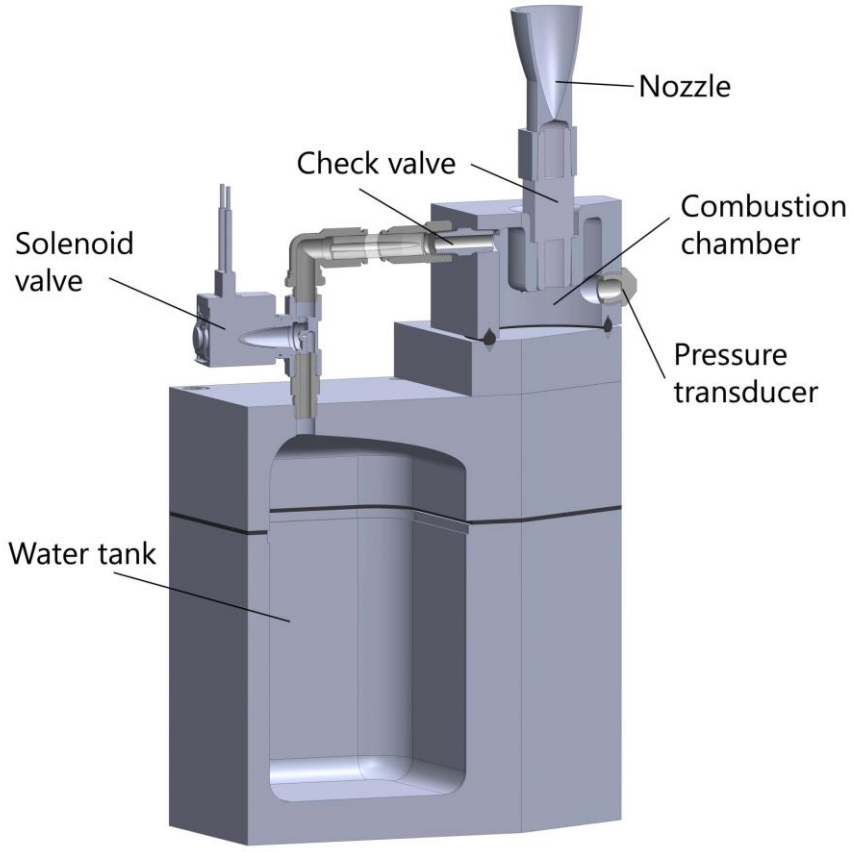

Figure 7. Cutaway of prototype electrolysis propulsion system.

cutaway view of the prototype propulsion system, with the main components and sensors labeled.

The entire assembly is oriented such that the nozzle's axis of symmetry is perpendicular to the ground and so that firing causes a downward force. Force measurements are taken by two strain gauges mounted on a plate upon which the prototype assembly is set. Measurements are taken at millisecond intervals and the data is recorded through a data acquisition card outside of the thermal vacuum chamber. Pressure inside the combustion chamber is also monitored through a pressure transducer. Figure 8 shows the prototype and force measurement setup inside the thermal vacuum chamber.

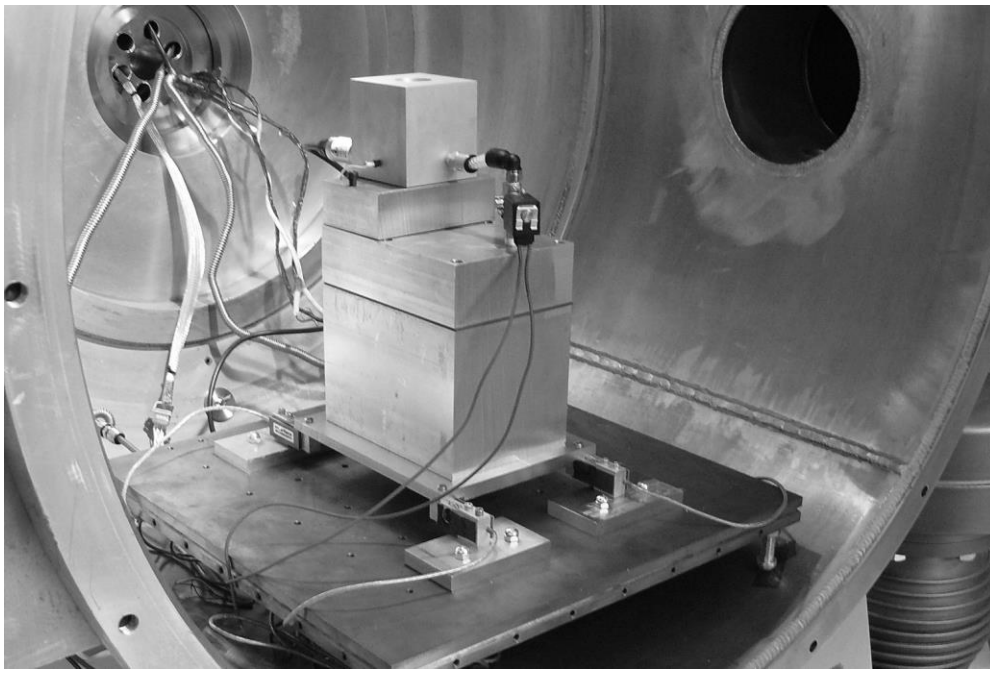

Figure 8. Prototype electrolysis propulsion system on thrust measurement assembly in Cornell's thermal vacuum chamber.

B. Measurements

Measurement of the power input for the electrolyzers is done by recording the voltage applied and current drawn throughout the electrolysis process. This allows for a measure of the amount of gas generated by the electrolyzers as given by Equation 1. The amount of gas in the chamber before a firing can be computed from the ideal gas law since pressure and temperature can be measured, the volume of the chamber is a known and fixed quantity, and the gases are assumed to be a stoichiometric mixture. The force data given by the strain gauges is integrated to compute the impulse in every pulse. The thrust generated by the engine and its specific impulse are related by

$$F = \dot{m} g_0 I_{sp} \quad (9)$$

Equation 9 can be integrated to obtain the impulse on left hand side, as shown in Equation 10. The equation can then be rearranged to compute an average specific impulse for the pulse, as given in Equation 11.

$$\int F \, dt = g_0 I_{sp} \int \dot{m} \, dt \quad (10)$$

$$I_{sp} = \frac{I}{g_0 \Delta m} \quad (11)$$

This measure of specific impulse is critical in sizing the water tank and, indirectly, the other components of the propulsion system for a given mission. The amount of fuel the spacecraft must carry is related to the total mission ΔV through the specific impulse, in the Tsiolkovsky rocket equation below.

$$\Delta V = I_{sp} g_0 \ln\left(1 + \frac{m_{prop}}{m_{sat}}\right) \quad (12)$$

C. Test results

Experiments at reduced pressure, conducted inside the vacuum chamber, yielded performance values for two of the configurations described in the *Basic Operation* section of Chapter 2. The two configurations that have been tested are the baseline configuration using a solenoid and two check valves, and the first alternate configuration using a high pressure solenoid valve. Of these two, specific impulse measurements are only obtained for the baseline configuration, since the gas in the chamber can be readily measured. The results of these low pressure experiments are shown in Figure 9. The check valve after the combustion chamber was set at 65 psi to 85 psi during these firings, significantly above the chamber pressures that were measured. While no clear trend is apparent from this data, it is expected that both impulse and specific impulse will increase as the pressure in the chamber increases, especially when the chamber pressure is well-matched with the cracking pressure of the check valve.

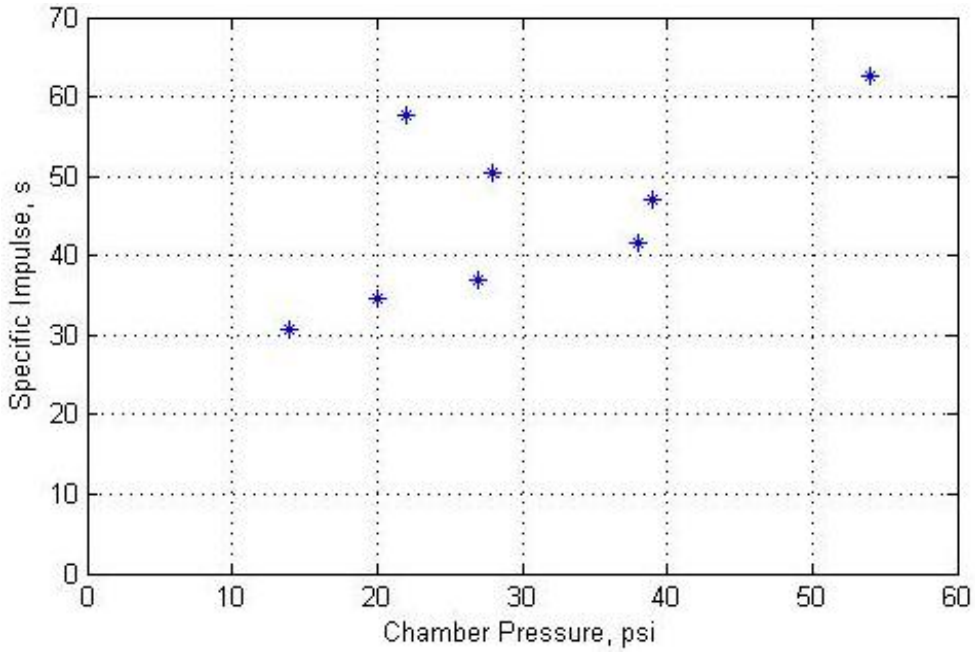

Figure 9. Chamber pressure vs. Specific impulse for the baseline configuration at low pressure.

Figure 10 shows the impulse from tests using both the alternate and the baseline configuration. The chamber pressure measurements for the alternate configuration are approximate, since the pressure in the chamber is transient and does not reach a stable value. This data shows that the impulse increases with the chamber pressure, although experiments at higher pressures will be necessary in order to reach the required performance for the system.

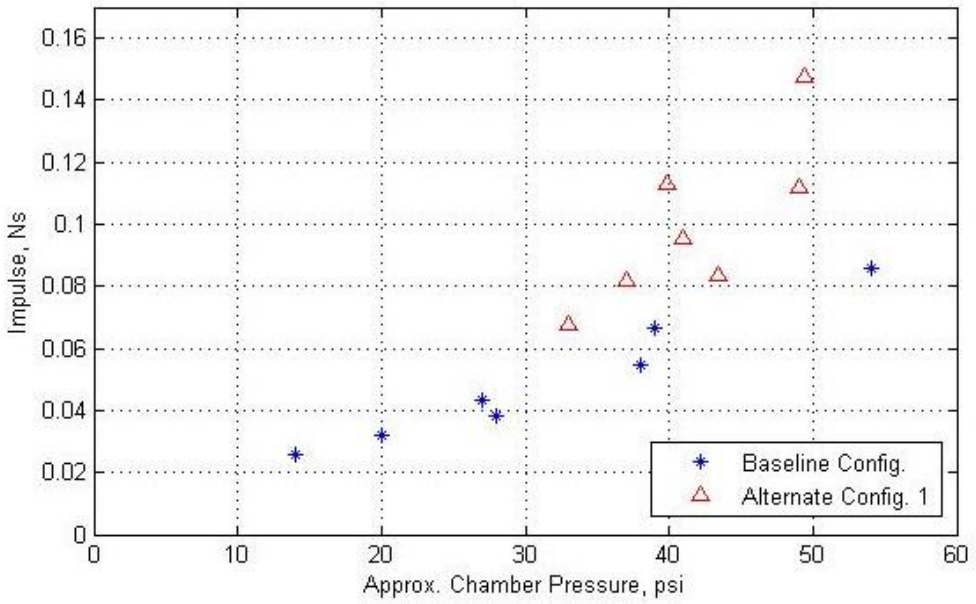

Figure 10. Chamber pressure vs. Impulse for the baseline and alternate configurations.

CHAPTER 3

ATTITUDE DYNAMICS AND CONTROL

The attitude dynamics necessary for the operation of the propulsion system seem to be complex and onerous at first glance. Spinning satellites, however, have a long history and are well-understood. Spinning while a thruster fires keeps the spacecraft from tumbling due to unwanted torques caused by misalignments. While these torques could be counteracted by the attitude control system, in CubeSats and other small spacecraft, a 3-axis attitude control system can be a large imposition. Such a system typically results in a significant fraction of the spacecraft devoted to reaction wheels or cold gas thrusters. Besides acting as the method of liquid-gas separation, by spinning the spacecraft significant reduction in the complexity of the system is achieved. This benefit is exemplified by the ability to reorient the spacecraft in any desired direction using only one cold gas thruster.

Satellite Dynamics and Attitude Requirements

A. Thrust axis spin rates for liquid-gas separation

A constant spin about the thrust axis separates the liquid water from the electrolyzed gases. This spin field obviates the need for the complex multi-tank storage systems proposed for large scale electrolysis propulsion systems and allows the CubeSat system to function with just one tank. The thrust axis spin can be actuated in several ways, although it must be such that the spacecraft has significant angular momentum in order to provide robustness in the presence of thruster misalignments.

This makes the use of reaction wheels or other actuators that don't exert external torques disadvantageous. For a system in a GTO mission, this thrust axis spin can be actuated using magnetic torquers. For interplanetary missions, magnetic actuators are ineffective and so a reaction mass system is required. Two systems are considered here, a 3U system operating at GTO and a 6U system operating near lunar orbit.

The choice of spin rate is driven by two factors, the Bond number (*Bo*) of the fluid and the required gyroscopic stiffness. The Bond number is a nondimensional parameter measures the relative importance of surface tension effects and inertial effects:

$$Bo = \frac{\Delta\rho \; a \; L^2}{\sigma} \qquad (13)$$

where $\Delta\rho$ is the difference in density between the water and the gas mixture, a is the magnitude of the acceleration due to the spacecraft spin, L is a characteristic length scale, and σ is the surface tension of the liquid. In the case of the 3U spacecraft described, the acceleration is approximately

$$a = \omega^2 r \qquad (14)$$

where ω is the spacecraft's spin rate, and r is the distance of the fluid's free surface from the center of mass of the spacecraft. In order for the inertial effects to dominate over the surface tension effects, and therefore for the gas bubbles to aggregate towards the inboard side of the tank, *Bo* should exceed unity. However, in order for inertial effects to be decidedly dominant, the goal is for *Bo* to be an order of magnitude larger, around 10 [22] [23].The minimum spacecraft spin rate is therefore

$$\omega = \left(\frac{Bo\ \sigma}{\Delta\rho\ r\ L^2}\right)^{\frac{1}{2}} \quad (15)$$

The distance from the center of mass of the spacecraft to the fluid free surface varies as propellant is spent, and the characteristic length is taken to be 0.09 m, the width of the tank. The density difference, $\Delta\rho$, between water and a stoichiometric mixture of hydrogen and oxygen gas can be approximated by the density of water (998.6 $\mathrm{kg/m^3}$), since even at the 10 bar pressure inside the tank, the density of the gas mixture is about two orders of magnitude lower than the density of water. The surface tension of water, σ, is 0.0728 N/m. The resulting spin rate necessary to attain a minimum Bond number of 10 would be largest when the free surface of the water is closest to the center of mass. This occurs at the beginning of the mission, when the tank is full and the center of mass is shifted closer to the propellant. For the GTO CubeSat, the distance is 70.3 mm, while for the Lunar CubeSat the minimum distance is 27.7 mm. Using these parameters, the minimum spin rate for the GTO CubeSat is 1.13 rad/s, or about 10.8 RPM, while for the Lunar CubeSat the spin rate must be larger than 1.80 rad/s (17.2 RPM).

B. Spin rates for attitude stability in the presence of shifts in the center of mass

As propellant is expended from the liquid water tank, the mass properties of the spacecraft change. The largest effect from this change is the shift in the position of the center of mass of the spacecraft. This effect produces a torque when the propulsion system fires because of the misalignment between the center of mass and the thrust axis. This torque can have a large impact on the rotational dynamics of the spacecraft. The thrust-axis spin provides passive robustness to torques caused by the main

thruster, environmental torques, and misalignments of both the jet of water vapor and mechanical features.

The center of mass for both spacecraft can be estimated by analyzing CAD models of the spacecraft. While simple aggregated mass models can be considered and have been analyzed in previous works, it is simpler and possibly more accurate to use the mass properties from a CAD model. As the mass properties change with fill fraction, the CAD models can account for the shift in center of mass even for complex tank shapes, as is the case in the Lunar CubeSat design. The relevant information to compute the effect of the center of mass shift is the distance between the center of mass and the spacecraft's thrust axis. This distance is the moment arm of the torque that results from firing a thruster not centered on the CM. The center of mass shift for the 3U GTO CubeSat results in a maximum moment arm of 8.3 mm, while for the Lunar CubeSat, the maximum moment arm is 24.4 mm.

The torque imparted on the spacecraft due to a thrust-axis misaligned with

Table 1. Spacecraft approximate principal moments of inertia for GTO CubeSat.

	Empty Tank	Full Tank
$\boldsymbol{I_{xx}}$	$\mathbf{0.0071\ kg\ m^2}$	$\mathbf{0.0075\ kg\ m^2}$
$\boldsymbol{I_{yy}}$	$\mathbf{0.0409\ kg\ m^2}$	$\mathbf{0.0475\ kg\ m^2}$
$\boldsymbol{I_{zz}}$	$\mathbf{0.0415\ kg\ m^2}$	$\mathbf{0.0480\ kg\ m^2}$

Table 2. Spacecraft approximate principal moments of inertia for Lunar CubeSat.

	Empty Tank	Full Tank
$\boldsymbol{I_{xx}}$	$\mathbf{0.0107\ kg\ m^2}$	$\mathbf{0.0130\ kg\ m^2}$
$\boldsymbol{I_{yy}}$	$\mathbf{0.0474\ kg\ m^2}$	$\mathbf{0.0576\ kg\ m^2}$
$\boldsymbol{I_{zz}}$	$\mathbf{0.0498\ kg\ m^2}$	$\mathbf{0.0613\ kg\ m^2}$

respect to the spin axis causes the spacecraft's angular momentum vector to precess. The thrust is approximately 4 N, and each burst lasts approximately 0.5 s. The torque imparted on the spacecraft when the moment arm is largest is in the *y*-direction in the body-fixed coordinates, and has a magnitude of 0.0334 Nm for the 3U CubeSat and 0.0977 Nm for the Lunar CubeSat. For the worst case of an instantaneous thrust impulse, the change in angular momentum is

$$\Delta \boldsymbol{H} = \boldsymbol{\tau} \Delta t \tag{16}$$

where $\boldsymbol{\tau}$ is the torque on the spacecraft and Δt is the time during which the pulse is applied. In this case, the total change in angular momentum is 0.0167 Nms for the GTO CubeSat and 0.0489 for the Lunar CubeSat. The angular momentum of the spacecraft is given by

$$\boldsymbol{H} = \boldsymbol{I} \cdot \boldsymbol{\omega} \tag{17}$$

where $\boldsymbol{I}$ is the spacecraft's inertia dyadic. For the GTO 3U CubeSat, the principal moments of inertia are as indicated in Table 1; for the Lunar CubeSat, the principal moments are in Table 2. In both cases, the principal moment of inertia aligned with the thrust axis, I_{zz}, is larger than I_{yy}, in order for the spin about the thrust axis to be stable. The angular velocity $\boldsymbol{\omega}$ is in the principal *z*-direction, which is as closely aligned as possible with the *z*-axis in body coordinates. We will consider the case of no products of inertia; i.e., the inertia matrix is diagonal in body coordinates. In that case, the angular momentum vector $\boldsymbol{H}$ is also in the *z*-direction. Since the torque and the momentum vectors are orthogonal, the change in angular momentum tilts the momentum vector by an angle

$$\theta = \tan^{-1}\left(\frac{|\Delta \boldsymbol{H}|}{|\boldsymbol{H}|}\right) \quad (18)$$

Rearranging Equations 16-18 yields the rotation speed in the *z*-direction as a function of the desired maximum precession angle:

$$\omega_z = \frac{\tau \Delta t}{I_{zz} \tan(\theta)}. \quad (19)$$

For both missions, a precession angle of 10 degrees or smaller is desired. In the case of the GTO CubeSat, this requires a rotation rate of 1.95 rad/s. The Lunar CubeSat must spin somewhat faster to achieve the same maximum precession angle – its rotation rate must be 5.86 rad/s. These rotation rates, however, are conservative in that the assumption of an instantaneous torque results in a higher spin rate than necessary, and in both cases the analysis takes into account the worst-case shift in the center of mass. If the torque is applied for a significant fraction of the spin period, the torque direction constantly changes. This reduces the precession angle. If the spacecraft were to complete an entire rotation in the time it takes to pulse the thruster, then the effects of that torque on the spacecraft's spin axis would cancel. The assumption of impulsive torque therefore represents a bounding case. The actual duration of the impulses is approximately 0.5 s, which is 16% of the GTO CubeSat's spin period and 46% of the Lunar CubeSat's spin period.

Besides the effects of the center of mass motion, an uneven mass distribution causes the inertia matrix to contain products of inertia, which introduce wobble into the spacecraft's motion (a constant tilt, as seen in the body axes). When products of inertia are present in the inertia tensor as described in body axes, the spacecraft's angular momentum vector is not aligned with the desired equilibrium spin axis, and

therefore the thrust pulses can cause the spacecraft to further precess if the wobble complements some other, existing angular bias.

Analysis of the products of inertia estimated using CAD models of the two spacecraft provides approximate values of the deviation between the spacecraft's principal axes and its body axes. For both spacecraft, the angle between the principal axis associated with the largest principal moment of inertia and the *z*-axis is shown in Table 3. These discrepancies can be mitigated in several ways. The placement of internal components such as avionics boards, antennas or batteries can be revised and modified in order to change the mass distribution. However, it is likely that the mass properties of the spacecraft's components in the CAD models are not accurate enough for this approach to be completely effective. Small ballast masses can also be placed to help balance the CubeSat, provided that enough margin exists in the mass budget. Another approach would be to align the thruster's axis of symmetry as closely as possible with the estimated principal axis, thereby reducing the impact of the spacecraft's wobble on the propulsion system's performance. A combination of these methods can be used in the final design and integration steps of the CubeSat, minimizing the misalignment between principal and body axes.

Table 3. Maximum angular deviation of spacecraft body z-axis from largest principal axis in CubeSat CAD model.

GTO CubeSat	**2.42 deg.**
Lunar CubeSat	**2.38 deg.**

Thrust axis spin actuation

A. GTO mission magnetic actuation

For a 3U mission that stays close enough to Earth such that the magnetic field is strong, the thrust axis spin can be actuated through magnetic torquers. Magnetic torquers can be embedded in the solar panels to save space, and have been used on many CubeSat missions. However, the use of magnetic torquers in GTO presents a few complications. Earth's magnetic field drops as $1/r^3$, where r is the distance from Earth's center. A GTO orbit would take the spacecraft from LEO altitude, approximately 7,000 km from Earth's center, to GEO altitude, 42,160 km away. The magnetic field is 218 times weaker at GEO. The applicable torque, which is proportional to the magnitude of the magnetic field and the magnitude of the torquer's magnetic moment, would therefore decrease just as much. In the initial GTO orbit, the magnetorquers will only be able to effectively torque the spacecraft during a fraction of the orbit near perigee. Since the velocity of the spacecraft is higher when near perigee, the time spent in the portion of the orbit where actuation is possible is small. The torque applied by a magnetorquer is

$$\boldsymbol{\tau}_M = \boldsymbol{M} \times \boldsymbol{B} \tag{20}$$

where $\boldsymbol{M}$ is the magnetorquer's magnetic moment and $\boldsymbol{B}$ is the Earth's magnetic field. [24] The magnitude of the torque can be estimated by using a dipole model of the Earth's magnetic field and the approximate values of magnetic moment of the magnetorquer coils. At perigee, the maximum magnitude of available torque is $|\boldsymbol{\tau}_M| = |\boldsymbol{M}| \cdot B_0 \left(\frac{R_E}{r}\right)^3$, where B_0 is the magnitude of Earth's magnetic field at the

magnetic equator. For a typical magnetorquer embedded in the solar panels of the CubeSat, [25] [26] magnetic moments are approximately 0.13 Am^2 for a 3U panel and 0.038 Am^2 for a 1U panel. This combination yields a maximum torque of $4.04 \times 10^{-6}\ N$. At a spin speed of 2 rad/s, it would take an actuator applying this maximum torque seven minutes, a small fraction of a GTO orbit, to reorient the spacecraft 1 degree. In order to command a control torque on the spacecraft, the magnetorquer is given a current command. Equation 20 can be used to solve for the magnetic moment by taking the cross product of the magnetic field $\boldsymbol{B}$ with Equation 20 and then expanding the right hand side using the triple product identity.

$$\boldsymbol{B} \times \boldsymbol{\tau}_M = \boldsymbol{B} \times (\boldsymbol{M} \times \boldsymbol{B}) = B^2 \boldsymbol{M} - (\boldsymbol{B} \cdot \boldsymbol{M})\boldsymbol{B} \quad (21)$$

Because components of the magnetic moment in the $\widehat{\boldsymbol{B}}$ direction do not contribute to torque, $\boldsymbol{B} \cdot \boldsymbol{M} = 0$**,** and Equation 21 reduces to

$$\boldsymbol{B} \times \boldsymbol{\tau}_M = B^2 \boldsymbol{M} \quad (22)$$

The magnetic moment required to produce a given control torque is therefore

$$\boldsymbol{M} = \frac{\boldsymbol{B} \times \boldsymbol{\tau}_M}{B^2} \quad (23)$$

This magnetic moment is produced by applying a voltage on the looped traces of known area embedded in the solar panels, which causes a current that generates the magnetic moment. The voltage required can be found from the pseudoinverse of a matrix representing the area of each loop and its normal vector.

B. Lunar CubeSat separation maneuvers

For the lunar CubeSat mission, and any other missions that begin far from LEO, the use of magnetic torquers is impractical. Internal momentum exchange devices such as reaction wheels or CMGs could generate the kinematics necessary to separate water from gas but do not provide the momentum stiffness required for the spacecraft. A method of generating a thrust axis spin in the 6U mission involves having two 3U satellites pushing off against each other, resulting in the satellites rotating at a nearly-equal and opposite rate. Before the two spacecraft deploy, they fit together to occupy the volume of a 6U CubeSat and fit within the constraints and specifications of the 6U P-POD. They are held together by a deployment mechanism on one end and a pivot joint on the other. A Ni-chrome burn wire activates the mechanism and springs cause the spacecraft to rotate in opposite directions. The pivot joint on the opposite end releases at a pre-set angle, allowing the two spacecraft to separate without impacting. Appropriately chosen spring constants lead to the desired spin rate. Any misalignments resulting in out-of-plane torques would cause initial angular velocities that are not well-aligned with the maximum principal moment of inertia. However, energy dissipation caused by the liquid propellant onboard assures that the spacecraft soon settles into a major axis spin.

Each individual spacecraft does not need to conform to the 3U volume specifications, although before the release sequence they fit together into a 6U volume. In the case of the planned lunar mission, the spacecraft are L-shaped, which provides more volume for the liquid water tanks and extends the ΔV capabilities of each spacecraft. The shape of the spacecraft also allows for the ratio between the

maximum and minimum principal moments of inertia to be greater, providing more stability when compared to the 3U spacecraft. Additionally, using the release to generate the rotation means the spacecraft can begin operating much sooner than in the magnetorquer case, something critical for the lunar mission.

Reorientation Maneuvers for GTO and Lunar CubeSat

Besides achieving the correct rotation rate, the spacecraft must also align its thruster in the direction necessary for firing. In the GTO mission, this is best achieved with magnetic torquers before the full rotation rate is achieved. Once the spacecraft is oriented correctly, the magnetorquers can begin the spin-up maneuver. The spacecraft is then correctly aligned at perigee, and any small deviations from this alignment can be corrected using the magnetorquers while near perigee. The Lunar CubeSat takes a very different approach, using a cold gas thruster to reorient the spacecraft. The direction of required thruster firings is not as predictable for this mission, which therefore requires that the spacecraft be able to reorient on demand, possibly several times during the course of the mission.

A. Numerical simulation of magnetorquer actuation

The 3U CubeSat in a GTO mission must reorient initially, before beginning the actuation for thrust axis spin. In order to reorient, the spacecraft would first attempt to drive the initial angular velocity imparted during separation from the P-POD to zero. The exact number of orbits needed to complete this maneuver depends on the spin state of the spacecraft when it separates. The maximum expected value of spin rate after separation is 0.122 rad/s. However, the spin rate of a previous CubeSat mission with unexpectedly large spin rate at separation was about 5.6 rad/s [27]**.** Reducing this

rotation rate to zero could require up to 60 orbits. Because the CubeSat contains liquid water in the propellant tank, liquid damping tends to bring the spacecraft into a stable spin about its axis of greatest inertia. If the spacecraft happens to be deployed with a similarly large rotation rate, it will transition into a major axis spin, which in some cases can allow the spacecraft to immediately initiate the thrust axis spin by either increasing or decreasing its spin rate to 2 rad/s.

A simulation of the attitude dynamics of the GTO satellite has been implemented in MATLAB/Simulink. The simulation includes closed-loop control of the satellite based on magnetorquers embedded in the solar panels, as described in Equations 20-23. The closed-loop control is implemented as a PD controller. The magnetic moments used in the simulation are those produced by the 1U and 3U solar panels available from GomSpace [26]. The simulation starts at perigee and propagates the orbit and attitude of the satellite subject to magnetic control torques. The magnetic field model used is the 1995 International Geomagnetic Reference Field (IGRF). The satellite's orbit is a geostationary transfer orbit with perigee at an altitude of 700 km.

The simulation was repeated 100 times in a Monte Carlo analysis, each time starting from a random spin state meant to simulate the uncertainty in the spin rate after separation from the P-POD. In all cases, the spin rate in each axis had a magnitude of at most 0.5 rad/s, several times larger than the likely separation spin rate of 7 deg/s (0.122 rad/s) [28]. The controller then attempted to reduce the spin rate to zero in as little time as possible, taking into account the hardware limitations in the form of actuator saturation. Results from these simulations are shown in Figure 11 and Figure 12. The first plot shows the component of the angular-velocity vector about the axis of maximum inertia for all 100 runs of the simulation. Because of the liquid damping, which is implemented in the simulation as a Kane damper [29]**,** the satellite stabilizes into a major axis spin within the first orbit. While this is approximately the behavior expected, it should be noted that the simulation is not meant to model the liquid motion exactly; such a model would require extensive test data to validate the complex liquid behavior [23]**.** Instead, simple damping is meant to capture the main

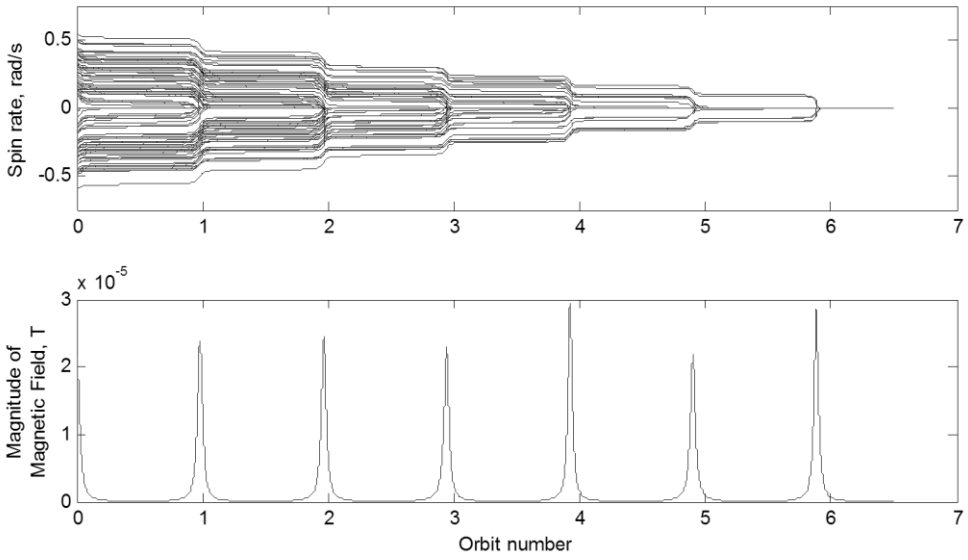

Figure 11. Simulation of satellite de-spin maneuver using magnetorquers.

effect the liquid will have on the spin state of the spacecraft. The nutation-damping time constant for this simple model can be matched to test data to represent a particular flight configuration.

The second plot shows the strength of the magnetic field at the satellite's position throughout the simulation. Because the actuators can apply only limited current, the strength of the magnetic field limits the maximum torque that can be applied. The local magnetic field is much stronger when the spacecraft is close to perigee and drops off approximately as r^{-3}. Therefore, the majority of the change in spin rate occurs when the spacecraft is near perigee. This fact can be used to implement a control algorithm that only actuates when the spacecraft is within some angular distance of perigee.

The distribution of the final spin rates about the principal axes for 100 runs of the simulation is shown in Figure 12. The controller is able to keep the final rotation rate to within 5×10^{-4} rad/s about all three axes.

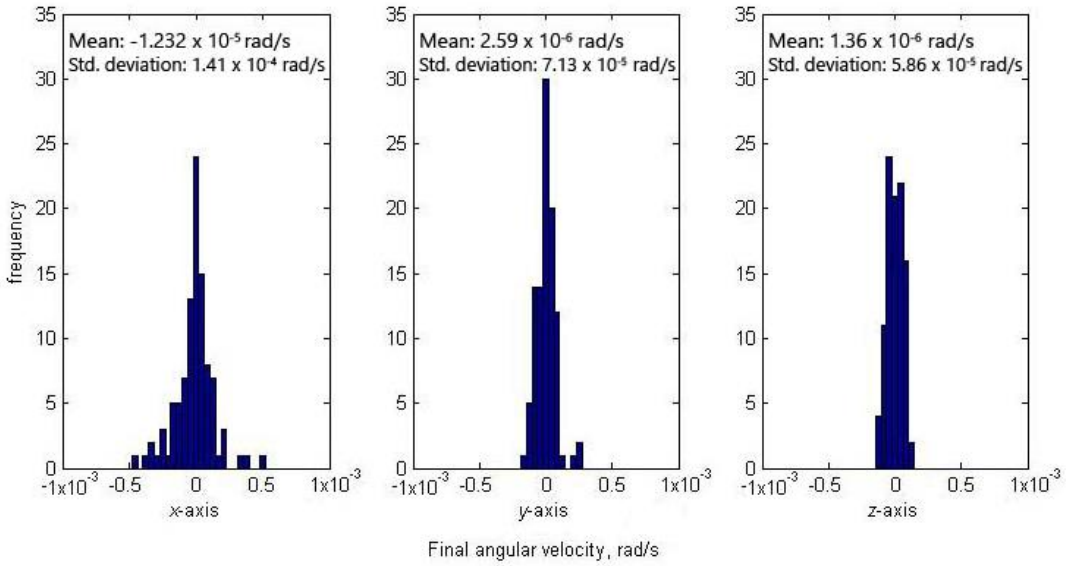

Figure 12. Distribution of final angular velocity of the satellite about each principal axis for 100 runs.

B. Reorientation for Lunar CubeSat

Unlike the 3U CubeSat, the Lunar CubeSat does not change its orbit by firing only at perigee. The Lunar CubeSat's orbit is similar to a single orbital transfer, including first a lunar gravity assist to achieve lunar orbit. This trajectory involves mid-course corrections, which could require the thruster to fire in arbitrary directions. Therefore, the satellite cannot rely on its gyroscopic stability to point in the correct direction for firings. Far outside the distance in which magnetic torquers are effective, the CubeSat must rely on cold gas thrusters to reorient. Since the spacecraft is spinning, only one cold gas thruster is needed per spacecraft, mounted such that it exerts torques normal to the angular momentum vector. Torque pulses applied once per spin period at the same angle in the rotation phase cause the angular momentum vector to precess. The fluid damping from the spacecraft would then assure that the spacecraft settles into a major axis spin about the new angular momentum vector, effectively reorienting the spacecraft. In this reorientation scheme, there is no control of the rotation rate about the thruster axis, as the thruster cannot apply a torque about that axis. However, changing the rotation rate is not necessary for the mission. The reorientation maneuver is intended to change the direction in which the main thruster fires while keeping the rotation rate constant.

Cold gas thruster systems for attitude control at the CubeSat scale are not commercially available in the form factor required for the satellite. However, it is possible to adapt off-the-shelf components to an existing microthruster to create a cold gas attitude control system suitable to the Lunar CubeSat. The thruster chosen is the Moog 58-149, which can provide a thrust of 3.56 N and a 3.5 ms response time using

30 W. The thruster has a very small envelope, allowing it to easily fit in the Lunar CubeSat. The fast response time assures that the on time of each pulse is small compared to the rotation rate of the satellite, while a large thrust means that the reorientation maneuvers take only a small amount of time to complete. The propellant to be used is compressed CO_2, which has a specific impulse of 61 s. Small CO_2 cylinders are readily-available off the shelf and can hold 38g of propellant at 2750 psi. The use of commercially-available cylinders instead of custom-made pressure vessels decreases the risk to primary payloads and reduces the total cost of the system.

The cold gas thruster is placed approximately 183 mm away from the center of mass of the spacecraft at the end of the mission. With this moment arm, the thruster can apply a torque of 0.06515 Nm. The pressure of the gas fed to the thruster is regulated to 87 psi, which allows the thruster to operate below its maximum pressure. The thrust provided by the system is therefore constant until the tank pressure falls below 87 psi, at which point it linearly decreases until the system runs out of propellant. For the regulated portion of the operation, the mass flow rate can be calculated based on the thrust and specific impulse of the system.

$$\dot{m} = \frac{F}{I_{sp}\, g_0} = 5.95 \times 10^{-4}\ kg/s \qquad (24)$$

Since the tank contains 38 g of propellant, the total time to empty the tank is

$$t = \frac{m_{prop}}{\dot{m}} = 63.9\ s \qquad (25)$$

The total impulsive change in angular momentum provided by the system is therefore

$$\Delta H = \tau \cdot t = 4.163\ Nms \qquad (26)$$

The cumulative reorientation angle is approximately the change in angular momentum divided by the total angular momentum of the spinning spacecraft.

$$\varphi = \frac{\Delta H}{H} = \frac{4.163\ Nms}{(6\ rad/s)(0.0341\ kg\ m^2)} = 20.35\ rad \qquad (27)$$

This angle is merely a metric that allows mission architectures to be assessed. No individual reorientation maneuver would be this large. In the case of the Lunar CubeSat, the performance is adequate for the amount of attitude control expected.

Analysis of External Torques on Rotating Satellite

Environmental disturbance torques that act on the satellites can cause the spin axis to precess, leading to an undesired thrust-vector direction. A high enough spin rate can stiffen the spacecraft's response to the point where disturbance torques cause negligible changes in the spacecraft's angular momentum. If the disturbance torque is significant, it must be compensated by the magnetic torquers or cold gas thruster in order to keep the spin axis properly aligned. The two major torques that act on the spacecraft are torques due to the gravity gradient and solar pressure.

A. Gravity Gradient Torque

Gravity gradient torques are only relevant for the GTO satellite, as the Lunar CubeSat is far beyond the region where this effect is important. Assuming that the geometric center of the spacecraft is coincident with the center of mass, the torque due to gravity gradient effects is approximately

$$\boldsymbol{\tau}_{GG} = \frac{3\mu}{r^3}\ [\hat{\boldsymbol{r}}_{\boldsymbol{sat}} \times (\boldsymbol{I} \cdot \hat{\boldsymbol{r}}_{\boldsymbol{sat}})] \qquad (28)$$

where $\boldsymbol{\tau}_{GG}$ is the gravity gradient torque, $\boldsymbol{I}$ is the inertia dyadic for spacecraft, μ is the Earth's gravitational parameter and $\boldsymbol{r}_{\boldsymbol{sat}}$ is the spacecraft's position from the earth's center [24]**.** The magnitude of the torque depends on both the distance from the center of Earth and the orientation of the CubeSat. At the approximate initial operating distance of the Lunar CubeSat, the scalar term associated with the distance from the center of the earth, $\frac{3\mu}{r^3}$, is $2.19 \times 10^{-6}\ s^{-2}$, whereas that value in low earth orbit is approximately $4 \times 10^{-6}\ s^{-2}$. The spacecraft spends relatively little time at the initial operating distance. Near the moon, the scalar term reduces to $2 \times 10^{-11}\ s^{-2}$. An analysis of the vector term ($[\hat{\boldsymbol{r}}_{\boldsymbol{sat}} \times (\boldsymbol{I} \cdot \hat{\boldsymbol{r}}_{\boldsymbol{sat}})]$) in the planar case (no component of $\hat{\boldsymbol{r}}$ in the direction of the principal axis closest to the body $\hat{z}$ axis) shows that the maximum value of that term is $0.5(I_{yy} - I_{xx})$. This makes the worst-case initial torque on the spacecraft $4.88 \times 10^{-8}\ Nm$ and the torque closer to lunar orbit $4.46 \times 10^{-13}\ Nm$. These torques would cause a change in the direction of the momentum vector of 0.0115 rad/day at the initial operating distance and 1.04×10^{-7} rad/day near the moon.

For the GTO CubeSat mission, the CubeSat's minor axis of inertia (its principal axis closest to the *x* body axis) must be aligned with the radial direction at perigee in order for the thrust pulses to be in the velocity direction. As the spacecraft orbits, this axis is no longer aligned with the radial direction in the Earth's frame, causing a torque. The gravity gradient torque for such an orbit is periodic, as shown in Figure 13. The change in angular momentum caused by this torque through an entire circular orbit would be zero. It is, nevertheless, important to quantify the precession

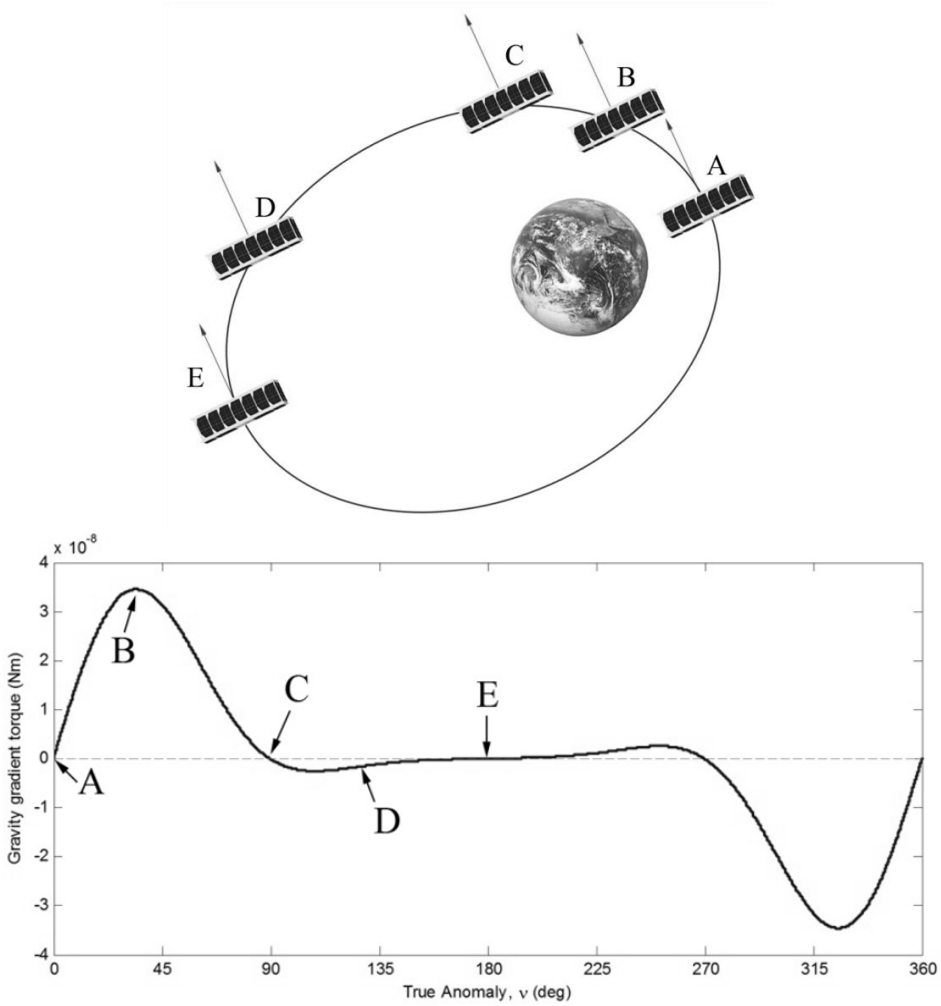

Figure 13. Gravity Gradient Torque for One Orbit. *The direction and magnitude of the gravity-gradient torque change throughout the initial orbit. Torque is in the direction normal to the page.*

caused by the periodic torque. This can be done by applying Equation 28 over one quarter of the orbit. The largest torque will occur in the interval between $\nu = 0$ and $\nu = \frac{\pi}{2}$ (as well as in the interval between $\nu = \frac{3\pi}{2}$ and $\nu = 2\pi$) since it is in those intervals when the spacecraft is closest to Earth. The gravity gradient torque in this case would be orthogonal to the *z*-direction, which causes the angular momentum vector to precess. The integral (over time) of the torque in Figure 13 for the portion of the orbit between $\nu = 0$ and $\nu = \frac{\pi}{2}$ is the change in momentum. The change in the orientation of the angular momentum vector given by Equation 18 is very small, 0.0007 rad.

B. Solar Pressure Torque

Torque on the spacecraft due to solar pressure is a much smaller effect than the gravity gradient torque. However, for a given orbit, the vector from the spacecraft to the Sun is nearly constant, which means the overall effect over one orbit can be of similar magnitude to the gravity gradient torque. The majority of the spacecraft's exterior is composed of solar cells with a high absorption coefficient. Therefore, the solar torque is approximated as only being due to absorbed radiation. The solar torque on the spacecraft can be expressed as

$$\tau_S = -\frac{F_{SC}}{c}\, C_A\, A\, d\left[\left(\hat{s}\cdot\hat{n}_y\right)\hat{z} + \left(\hat{s}\cdot\hat{n}_z\right)\hat{y}\right] \qquad (29)$$

where F_{SC} is the solar illumination constant, c is the speed of light, C_A is the coefficient of absorptivity, A is the illuminated area, d is the moment arm, $\hat{s}$ is the unit vector in the direction of the sun and $\hat{n}$ is a unit vector normal to the illuminated surface. A net torque will be produced only when there is an offset in the center of

gravity such that more area is illuminated on one side of the CG than on the other side. This is shown as the hashed area in Figure 14. The moment arm of the torque is the distance between the CG and the midpoint of the area A.

The alignment of the sun vector that produces the worst-case torque occurs when the sun vector is parallel to the $\hat{z}$ normal vector. The largest area A is attained when the spacecraft's center of gravity is at its maximum displacement from the spacecraft's geometric centroid. In this case, the torque has a magnitude of $7.62 \times 10^{-10}\ Nm$ in the positive or negative $\hat{y}$ direction. Integrated over an entire GTO orbit, the change in angular momentum of the spacecraft is $2.87 \times 10^{-5}\ Nms$, which leads to a precession angle of 0.0003 rad.

A similar analysis can be done for the Lunar CubeSat, which spends significantly more time in a given orientation, and is therefore more susceptible to the change in angular momentum due to the long term effects of solar pressure. These changes in momentum must be compensated for by the attitude control system.

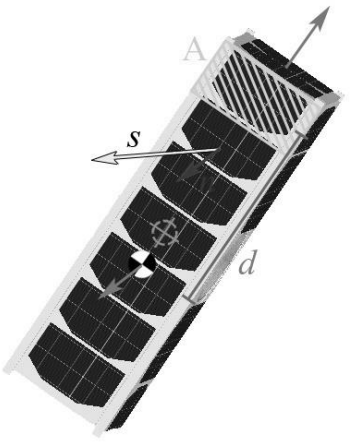

Figure 14. Solar torque acting on the rotating spacecraft.

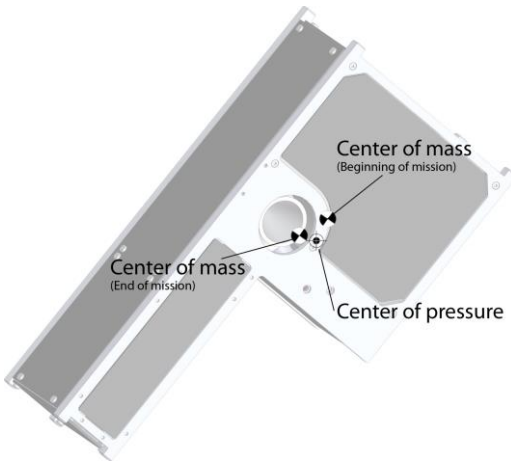

Figure 15. Approximate location of the centers of mass and center of pressure for the Lunar CubeSat.

However, since the attitude control system can only compensate for torques normal to the spin axis, care must be taken to assure that the solar torques do not cause the spacecraft rotation to slow down (or speed up) significantly. The component of the solar torque on these faces can be modeled as a single force acting at the center of pressure with a moment arm that is the distance between the center of mass and the center of pressure. Since the location of the center of pressure changes as the spacecraft spins, the torque exerted by the solar pressure is time-varying. The component of the solar torque in the *z*-direction is shown in Figure 16 for two rotations at the beginning and the end of the mission. In both cases, the change in angular momentum sums to zero over the course of a single rotation. Over half of a spin period, the maximum change in angular momentum is 2.3×10^{-9} Nms, which corresponds to a change in the spin rate of 3.8×10^{-8} rad/s.

Torque due to solar pressure on the faces of the satellite normal to the *x*- and *y*-axes results in precession of the angular momentum vector. Through internal energy dissipation, this precession leads to a change in the direction of the angular velocity

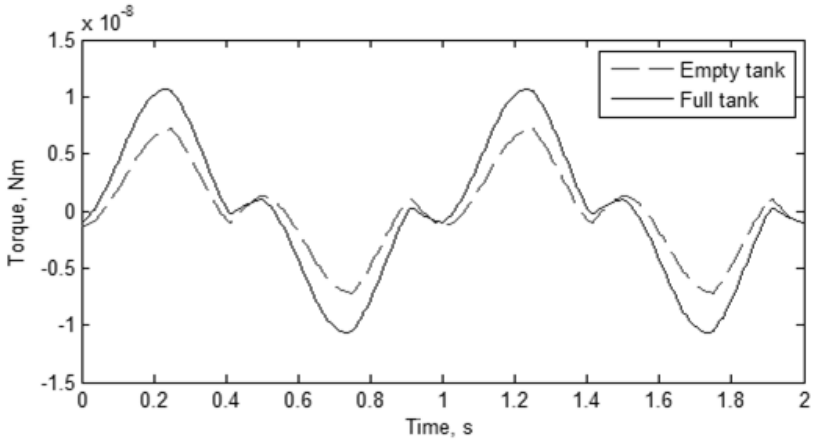

Figure 16. Solar torque about *z*-axis in Lunar CubeSat for two rotations.

vector (and therefore the satellite) in the inertial frame. For this cross section of the satellite in direct solar illumination, the torque is 3.34×10^{-9} Nm with a full tank and 7.34×10^{-10} Nm with an empty tank. In the worst-case scenario of the satellite at the beginning of the mission with a full tank and under constant direct illumination, the resulting change in the direction of the angular momentum vector would be 0.028 rad over the course of a month, a tilt that is not significant for the spacecraft's pointing ability.

CHAPTER 4

APPLICATIONS AND MISSION ARCHITECTURES

Electrolysis propulsion systems have direct applicability in secondary payload missions that require a large ΔV in a limited amount of time, as well as in spacecraft with limited power generation capabilities that also require ΔV. Electrolysis propulsion systems offer a number of important benefits, which are amplified when used on CubeSats or other secondary payloads. The system is safe at launch and poses no risk to the rocket or primary payload. This is because it has no pressurized containers at launch, no explosives or combustible propellant, and no toxic substances. Since the tank only contains liquid water at atmospheric pressure, there are no safety concerns associated with the propulsion system. Once in orbit, the system is also flexible from a power operations standpoint. The electrolyzers can operate at 2W, 4W or 6W, depending on the available power, and can be duty cycled to reduce power consumption if necessary, with no reduction in specific impulse or total ΔV. The only drawback to operating at a lower power is that it takes more time to generate the ΔV.

With these benefits in mind, one potential use of these propulsion systems is for lifetime extension of low Earth orbit CubeSats. At operating altitudes of 300 km, the propulsion system can extend the lifetime of a 3U CubeSat by at least 10 months. For a CubeSat at 400 km, the lifetime extension would be at least 4.5 years. This system can also provide drag compensation for CubeSats in very low orbits, allowing for science payloads to fly for extended periods of time in orbits that would otherwise decay in a few days or weeks. At 250 km, for example, a CubeSat's orbit could expect

to decay in 4.5 to 11 days. With an electrolysis propulsion system on board, the CubeSat could stay in orbit for anywhere between 3.5 months and 10 months [30].

Demonstrating technologies in space is a critical part of increasing the technology readiness level of a component. For CubeSat components this typically involves demonstration in low earth orbit. However, the NASA CubeQuest Centennial Challenge provides an ideal venue for demonstrating a CubeSat propulsion system. This challenge, meant to promote innovation necessary for interplanetary missions using CubeSats, offers a ride on board the first launch of NASA's Space Launch System (SLS). From this trans-lunar injection orbit, a satellite would need approximately 400 m/s of ΔV in order to capture in a stable orbit around the moon. The propulsion system sized for Cornell's Lunar CubeSat can provide in excess of 800 m/s, leaving sufficient margin for the uncertainties inherent in the initial orbit, mid-course corrections, and orbit capture maneuvers required for this mission. Not only is propulsion necessary for the Lunar Derby portion of the challenge, it is critical to have a propulsion system that can provide enough ΔV to place the CubeSat in lunar orbit in a limited amount of time. Because of the stringent demands on the propulsion system and the 6U form factor, this flight opportunity lends itself to the implementation of promising new propulsion systems at the CubeSat scale.

Mission Profile

The estimated initial conditions of the secondary payloads after deployment as announced by the CubeQuest and SLS teams places the CubeSats on earth escape trajectories. The CubeSats released from SLS would fly close to the moon and then into a heliocentric orbit. By imparting ΔV before the encounter with the moon, a

CubeSat would be able to change its orbit significantly. A gravity assist near the moon can place the spacecraft into an earth-centered orbit that is highly advantageous for subsequent lunar orbit insertion. In this way, the spacecraft would take advantage of the initial orbit and the lunar gravity assist to reduce the ΔV needed for lunar capture. Mid-course corrections would then take place near the apogee of the orbit. These burns could be in any arbitrary direction, which is why it is important for the satellite to have the reorientation capability that the cold gas thruster provides. With the cold gas thruster, the spacecraft can reorient to burn in any direction, and has a total reorientation budget of approximately 20 radians (1146 degrees). The trajectory of the spacecraft and the sequence of maneuvers necessary as simulated using STK are shown in Figure 17.

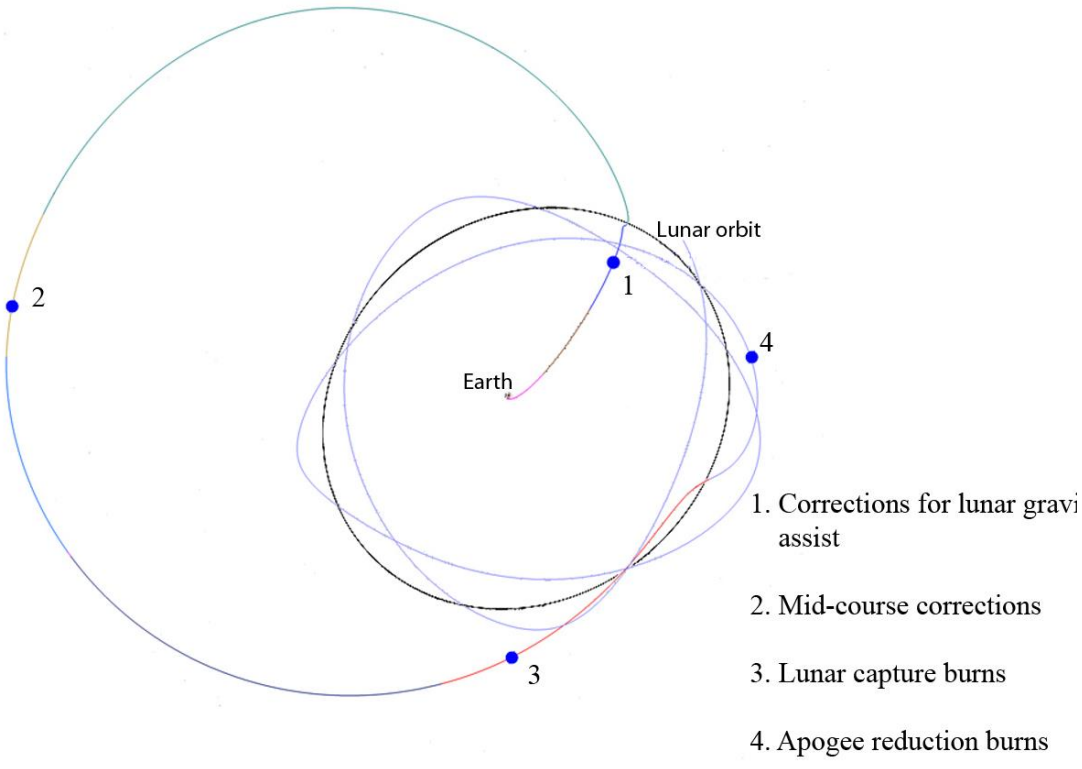

Figure 17. Orbit profile starting from an SLS deployment.

Satellite design

The operating environment and distance from Earth places requirements on the satellite that are different from those placed on a LEO CubeSat. These requirements affect the design of several subsystems, in some cases leading to solutions that are radically different than those in other CubeSats. Besides the propulsion system, which was described in Chapter 2, the subsystems that are significantly different from what would be found on a LEO CubeSat are outlined here.

A. Attitude Control

The attitude control and navigation system must provide an estimate of position and attitude that can be used by the satellite to reorient and fire its thruster. In a LEO CubeSat, this can be accomplished by several onboard sensors including magnetometers, GPS antennas, sun sensors or Earth limb sensors. The orbit of the satellite can also be determined by obtaining Two Line Elements (TLEs) from NORAD or similar radio ranging techniques. Once outside the GPS constellation, the only one of the sensors above that could provide useful information are sun sensors. Ranging data could also be used given sufficiently capable ground stations. Star trackers have been proposed for interplanetary CubeSats despite being expensive compared to the other sensors, but typically require that the spacecraft's angular velocity is very small.

The Lunar CubeSat uses a set of CMOS cameras to perform optical navigation using the centroids and apparent diameters of the Earth and Moon. The procedure used follows that outlined by Christian [31].The cameras can also be used as sun sensors, as they can provide the direction of the sun. The accuracy of these sensors is still being

determined, but the sensors are expected to provide a coarse attitude and navigation solution suitable for the pointing needs of the spacecraft.

The cold gas thruster described in Chapter 3 is the attitude actuator used to reorient the spacecraft. This single thruster can reorient the spacecraft in any direction while it is spinning, in a scheme that takes advantage of the rotational dynamics and energy dissipation of the spacecraft to obviate the need for an attitude control system with multiple thrusters.

B. Avionics

The design of the flight computer for the Lunar CubeSat is one that maximizes the use of commercial off the shelf parts in order to reduce cost and development time. The current design incorporates several microcontrollers to handle the image processing necessary for optical navigation as well as the functions of a flight computer. These microcontroller boards are based on the Texas Instruments MSP430 chips, which incorporate ferroelectric RAM and operate at very low power. An architecture with several microprocessors replacing the flight computer can also create redundancy in the event of failures or single upset errors caused by radiation.

C. Communications

The communications subsystem needs to be designed to operate at very large distances. In order to compensate for the free space loss associated with communicating from lunar distance, the link must include a large signal processing gain. This can be achieved through the use of error correction codes that increase the signal processing gain at the expense of bit rate.

The lack of fine pointing capabilities associated with a rotating satellite limits the possible gain associated with a narrow beamwidth approach, such as optical communications or a high gain antenna on the satellite. For the ground station, several options are being considered, including the ground stations used by previous Cornell nanosatellites and larger dishes available commercially.

The unique operating conditions and requirements of the propulsion system lead to a design that integrates the passive dynamics of the satellite in an effort to reduce complexity. The overall design of the satellite is shown in Figure 18. Two of the satellites fit together into a 6U form factor. They are separated by springs as described in Chapter 3 in order to generate the required rotation rates for propulsion and passive stability in the presence of external torques.

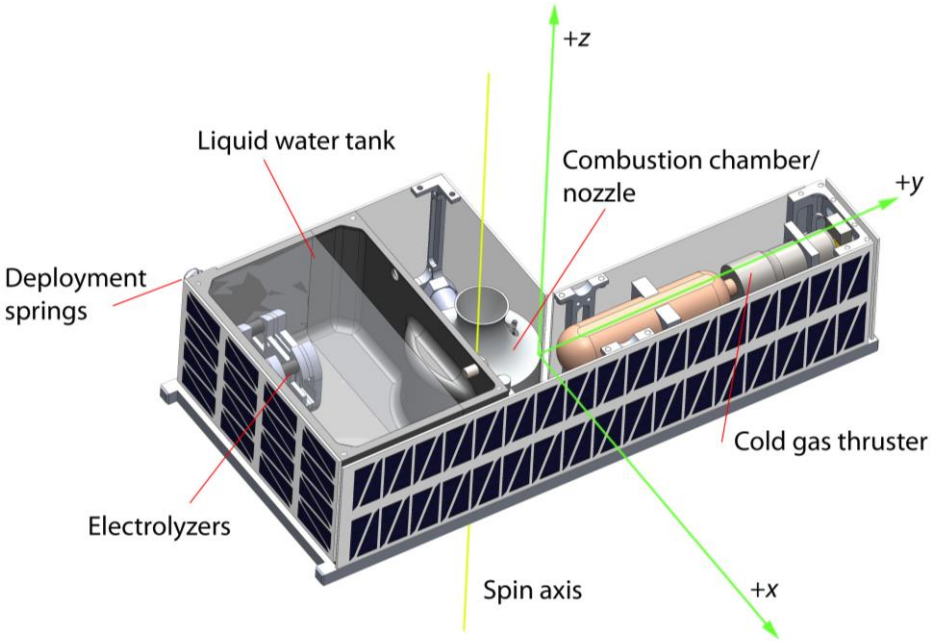

Figure 18. The Cornell Lunar CubeSat. Two of these satellites fit together to form a 6U CubeSat

CHAPTER 5

CONCLUSION

Propulsion systems designed for the CubeSat scale present an exciting opportunity to expand the capabilities of small satellites, both in LEO and deep space. The main contributions of this work help extend the field of available propulsion systems by presenting the architecture and design of a new type of propulsion system as well as example missions where these propulsion systems could be effectively demonstrated. This work also specifies how the dynamics of a satellite with liquid fuel can be leveraged to control the distribution of propellant, to simplify the attitude control system, and to provide gyroscopic stiffness in the presence of external torques.

Electrolysis propulsion systems take advantage of the small scale and restricted envelope of the CubeSat, providing a propulsion system that fits in naturally at the CubeSat scale and provides enough ΔV for missions beyond LEO. Unlike other propulsion systems at this scale, electrolysis systems use non-toxic propellant, do not use explosives, hypergolics or cryogenics, and have no pressurized tanks at launch. The ability to conform to CubeSat standards makes them an attractive option for future missions.

Electrolysis propulsion systems have benefits once in orbit as well. Because they can operate at low power, payloads or other subsystems can dominate the power budget and still allow the propulsion system to operate with however much power

remains. This flexibility in power use can in some cases allow satellites to use body-mounted panels instead of more complex deployable arrays.

Considering the passive attitude dynamics of the satellite in the design of the mission allows for further reduction in the complexity of the satellite. The spacecraft's spin not only separates the water from the gaseous propellants, but also provides gyroscopic stiffness that allows the spacecraft to minimize the effect of unwanted overturning torques—both environmental torques and torques caused by the thruster itself. The concept of operations leverages the fact that the spacecraft is a major axis spinner with significant energy dissipation to simplify its attitude control scheme. Because of the passive dynamics of the spacecraft, reorientation can be achieved with a single cold gas thruster instead of a 3-axis attitude control system. In small satellite and CubeSat missions, where all of the spacecraft subsystems are closely integrated, these reductions in complexity of subsystems can have a large impact. Besides demonstrating the propulsion system, the Cornell Lunar CubeSat is designed to showcase the benefits of integrating the dynamics of the satellite into its concept of operation.

The importance of a water-based propulsion architecture is also highlighted by the abundance of water in the solar system. While it may be somewhat inaccessible, water exists or is thought to exist in many of the moons of the outer planets, in the poles of the moon, Mercury and Mars, in comets and asteroids [32] [33]. Architectures that take advantage of in-situ resources could use water electrolysis as a method of generating propellant for exploration missions, reducing the mass that needs to be sent from Earth.

Analytical and numerical methods can be used to estimate the performance of electrolysis propulsion systems. Laboratory tests in a vacuum chamber can be used to demonstrate the performance and provide accurate parameters with which to design flight versions of these systems. However, it is important to test a propulsion system in space in order to flight-qualify the system and demonstrate its abilities. Flight opportunities in the near future, including the CubeQuest challenge, will provide important venues for verifying the performance of these systems and demonstrating their significance in the development of low-cost interplanetary CubeSat missions.

REFERENCES

1 Mueller, J., Hofer, R., and Ziemer, J. *Survey of Propulsion Technologies Applicable to CubeSats;* Jet Propulsion Laboratory, National Aeronautics and Space Administration: Pasadena, CA, 2010.

2 Staehle, R., Puig-Suari, J., Svitek, T., Friedman, L., and Blaney, D. "Interplanetary CubeSats: Some Missions Feasible Sooner than Expected," *1st Interplanetary CubeSat Workshop*, Cambridge, MA, 2012.

3 The CubeSat Program, Cal Poly SLO. *CubeSat Design Specification;* California Polytechnic State University: San Luis Obispo, CA, 2009.

4 Air Force Space Command. *Range Safety User Requirements Manual Volume 6;* Air Force Space Command, 2004.

5 Stechman, R. C. and Campbell, J. G. *Water Electrolysis Propulsion System;* Technical Report AFRPL-TR-72-132; The Marquardt Company: Van Nuys, CA, 1973.

6 Stedman, J. K., US Patent Application for "Regenerative Fuel Cell," No. 3,981,745, September 21, 1976.

7 Mitlitsky, F., Weisberg, A. H., Carter, P. H., Dittman, M. D., Myers, B., Humble, R. W., and Kare, J. T. "Water Rocket - Electrolysis Propulsion And Fuel Cell Power," *American Institute of Aeronautics and Astronautics Space Technology Conference and Exposition*, Albuquerque, NM, 1999.

8 Mitlitsky, F., de Groot, W., Butler, L., and McElroy, J. "Integrated Modular

Propulsion and Regenerative Electro-Energy Storage System (IMPRESS) for Small Satellites," *10th Annual American Institute of Aeronautics and Astronautics/Utah State University Conference*, Logan, UT, 1996.

9 Davenport, R. J., Schubert, F. H., and Grigger, D. J., "Space water electrolysis: space station through advanced concepts," *Journal of Power Sources*, Vol. 36, No. 3, 1991, pp. 235-250.

10 McElroy, J. F. US Patent Application for "Electrochemical hydrogen separator system for zero-gravity water electrolysis," No. 4,950,371, filed March 24, 1989.

11 de Groot, W. A., Arrington, L. A., McElroy, J. F., Mitlitsky, F., Weisberg, A. H., Carter II, P. H., Myers, B., and Reed, B. D. "Electrolysis Propulsion for Spacecraft Applications," *33rd Joint Propulsion Conference and Exhibit*, Seattle, WA, 1997.

12 de Groot, W. A., Maloney, T. M., and Vanderaar, M. J. "Power, Propulsion, and Communications for Microspacecraft Missions," *COSPAR Colloquium on Scientific Microsatellites*, Tainan, Taiwan, ROC, 1997.

13 Heidt, H., Puig-Suari, J., Moore, A., Nakasuka, S., and Twiggs, R. "CubeSat: A new Generation of Picosatellite for Education and Industry Low-Cost Space Experimentation," *USU Conference on Small Satellites*, Logan, UT, 2000.

14 Toorian, A., Diaz, K., and Lee, S. "The cubesat approach to space access," *Proceedings of the IEEE Aerospace Conference*, 2008, pp. 1-14.

15 Hevner, R., Holemans, W., Puig-Suari, J., and Twiggs, R. "An Advanced Standard for CubeSats," *AIAA/USU Conference on Small Satellites*, Logan, UT, 2011.

16 Zeledon, R. A. and Peck, M. A. "Electrolysis Propulsion for CubeSat-Scale Spacecraft," *AIAA SPACE 2011 Conference & Exposition*, Long Beach, CA, 2011.

17 Zeledon, R. A. and Peck, M. A. "Attitude Dynamics and Control of a 3U CubeSat with Electrolysis Propulsion," *AIAA Guidance, Navigation, and Control Conference*, Boston, MA, 2013.

18 Cullis, C. F. and Hinshelwood, C. N., "The Mechanism of the Hydrogen-Oxygen Reaction. IV. The Activation Energy of the Initiating Process," *Proceedings of the Royal Society of London. Series A, Mathematical and Physical Sciences*, Vol. 186, No. 1007, 1946, pp. 462-469.

19 Kuznetsov, M., Redlinger, R., Breitung, W., Grune, J., Friedrich, A., and Ichikawa, N. "Laminar burning velocities of hydrogen-oxygen-steam mixtures at elevated temperatures and pressures," *Proceedings of the Combustion Institute*, 2011, p. 895–903.

20 Spakovszky, Z. S. *Thermodynamics and Propulsion 16.Unified,* 61st ed.; Cambridge, MA, 2007.

21 Sutton, G. P. and Biblarz, O. *Rocket Propulsion Elements,* 7th ed.; John Wiley & Sons, 2001.

22 Hubert, C. and Swanson, D. "Surface Tension Lockup in the IMAGE Nutation Damper–Anomaly and Recovery," *Space Flight Mechanics Symposium*, NASA Goddard Space Flight Center, 2001.

23 Hubert, C. *Behavior of Spinning Space Vehicles With Onboard Liquids;* NASA/KSC contract NAS10-02016;, 2003.

24 Wertz, J. R. (Ed.). *Spacecraft Attitude Dynamics and Control,* Kluwer Academic Publishers, Dordrecht, ND, 1978. Chap. 17

25 Clyde Space. CubeSat Shop. http://www.clyde-space.com/cubesat_shop (accessed December 2012).

26 GomSpace. NanoPower Solar Panels. http://www.gomspace.com (accessed July 2013).

27 Ecole Polytechnique Federale de Lausanne. SwissCube News Update, 2011. SwissCube. http://swisscube.epfl.ch/ (accessed December 2012).

28 Nehrenz, T. *Initial Design and Simulation of the Attitude Determination and Control System for LightSail-1;* California Polytechnic State University: San Luis Obispo, 2010.

29 Peck, M. A. US Patent Application for "Momentum Stabilized Launch Vehicle Upper Stage," No. 20040135035, filed April 30, 2003.

30 Wertz, J. , Everett, D. F., and Puschell, J. J., Eds. *Space Mission Engineering: The New SMAD,* Microcosm Press, Hawthorne, CA, 2011.

31 Christian, J. A., "Optical Navigation Using Planet's Centroid and Apparent Diameter in Image," *Journal of Guidance, Control, and Dynamics*, Vol. 38, No. 2, 2015, pp. 192-204.

32 de Pater, I. and Lissauer, J. J. *Planetary Sciences,* 5th ed.; Cambridge University Press, Cambridge, 2001.

33 National Aeronautics and Space Administration. Water in the Solar System: Water,

Water, Everywhere! https://solarsystem.nasa.gov/yss/display.cfm?ThemeID=23 (accessed February 2015).

APPENDIX

GENERALIZED FRAMEWORK FOR LINEARLY CONSTRAINED CONTROL MOMENT GYRO STEERING[1]

Laura L. Jones[2], Rodrigo A. Zeledon[1], and Mason A. Peck[3]
Cornell University, Ithaca, NY, 14850

Constrained steering laws for control-moment gyroscope (CMG) arrays can avoid internal singularities without inducing torque error or requiring pre-computed momentum paths, making such steering laws worthy of further study. This paper proposes a generalized framework for constrained steering laws that are linear with respect to the gimbal rates by augmenting the system's Jacobian matrix with constraint equations. The derivation of this generalized framework is followed by a discussion of constraints used in laws of this type and general principles for designing a singularity-free constraint. A CMG array consisting of three scissored pairs provides an example of how a known steering law fits into this framework. A new steering law based on orthogonal triplets of single-gimbal CMGs is developed with the help of the

[1] This paper was published by the American Institute of Aeronautics and Astronautics, Inc. in the Journal of Guidance, Control, and Dynamics, Vol. 35, No. 4, July-August 2012.
[2] Graduate Student, Dept. of Mechanical and Aerospace Engineering, 129 Upson Hall Ithaca NY 14850, AIAA Student Member.
[3] Associate Professor, Dept. of Mechanical and Aerospace Engineering, 212 Upson Hall Ithaca NY 14850, AIAA Full Member.

proposed methodology. Simulations of the Violet nanosatellite's attitude-control performance verify the results of this new steering law.

Nomenclature

A	=	system matrix augmented with constraint law
α	=	scalar constant
β_1	=	scaling value for the first row of the Jacobian in the constraint equation
β_2	=	scaling value for the second row of the Jacobian in the constraint equation
β_c	=	non-zero scaling value for the cross-product component of the constraint equation
C	=	$m \times n$ matrix of general constraint equations relative to the gimbal rates
$\tilde{C}$	=	$m \times n$ matrix of general constraint equations relative to the gimbal angles
D	=	$m \times 1$ matrix of the solution to the constraint equations relative to the gimbal rates
$\tilde{D}$	=	$m \times 1$ matrix of the solution to the constraint equations relative to the gimbal angles
d	=	scalar term in the constraint equation
Δ	=	determinant of the A system matrix
h	=	magnitude of the angular momentum of an individual CMG
J	=	$3 \times n$ system Jacobian matrix
n	=	number of CMGs in an array
m	=	number of scalar constraint equations in a constraint-based steering law
Φ	=	$n \times 1$ matrix of gimbal angles (made up of ϕ_i)
$\dot{\Phi}$	=	$n \times 1$ matrix of gimbal rate commands (made up of $\dot{\phi}_i$)
ϕ	=	individual CMG gimbal angles

τ_C = commanded 3×1 matrix of torque scalars for spacecraft-body reference axes

τ_j = single, scalar torque component of τ_C

τ_{x_i} = the value of scalar x-component torque distributed to the *i*th triplet

Introduction

Control moment gyroscopes (CMGs) are momentum-exchange actuators used to control the attitude of a spacecraft. One or more gimbals tilt the CMG's rotor, and in doing so, the gimbal precesses the CMG's angular-momentum vector to produce a torque that is largely due to a kinematic constraint. Therefore CMGs require less power to produce the same torque than reaction wheels, which accelerate or decelerate the rotor instead. CMGs are particularly useful in applications requiring high slew rates or large torques. Although several types of CMGs exist, including variable-speed CMGs[1] and double-gimbal CMGs[2], the single-gimbal CMG (SGCMG) offers a combination of cost effectiveness and mechanical simplicity that makes it attractive for implementation in space systems[3]. This paper considers only single-gimbal CMGs and drops the "SG" from the acronym, in keeping with common practice. Since the rotor of a CMG gimbals about only one axis, it can provide only a single actuation degree of freedom. A minimum of three is necessary to achieve full attitude control instantaneously, although it is more common to use an array of four or more for singularity avoidance or redundancy purposes. A CMG array is controlled by a steering law, an algorithm that governs how the CMGs move within the array (usually via commanded gimbal rates) to provide the required three-axis torque. CMG steering laws determine the gimbal rates necessary for the CMG array in response to a torque

commanded by the attitude-control system for feedback control of the spacecraft attitude dynamics.

A significant drawback of CMG arrays is the presence of kinematic singularities at certain gimbal configurations. These singularities are points at which the array is incapable of instantaneously producing torque in a particular direction, which results in a loss of controllability. A major research focus in the community has been designing steering laws for CMG arrays such that an attitude-control system is capable of handling these singularities despite the practical hardware- and operations-related limitations of contemporary space systems.[4,5,6]

A certain class of CMG steering laws uses linear constraints (in hardware or software) to avoid singularities while finding an instantaneous solution without inducing error in the torque imparted to the spacecraft. Despite that several variations of this steering law exist in the literature,[7,8] a generalized form of this particular CMG steering law has yet to be presented. Once in a generalized form, the problem is freed from specific array geometries or constraint laws, which opens up the design space to the possibility of optimized configurations. This paper presents a generalized mathematical description of steering laws with linear constraints and uses the familiar array of three scissored pairs to explain the formulation. It then provides an example based on Cornell University's Violet nanosatellite, which uses six CMGs in triplet combinations, to demonstrate the validity of the formulation.

Background and Context for CMG Steering Laws

While CMG steering laws have been studied at length for decades, they are still an area of active research primarily because no one category of solutions appears to satisfy all of the requirements for an ideal steering law. Most published approaches to this problem fall roughly into one of six categories[9], although there is overlap: the Moore-Penrose pseudoinverse,[10] singularity-robust pseudoinverse and similar solutions,[11,12,13,14,15] offline-planning,[16] preferred gimbal-angle laws,[17] gradient or null-motion methods,[11,18,19,20] and constraint-based steering laws.[7,8] Each method has different advantages and characteristics, but a perfect solution has yet to be found[9]. Table 1 lists the characteristics of broad categories of steering laws and assesses them in terms of the attributes of ideal steering laws.

Even if a perfect steering law does not exist, describing the characteristics of such an ideal helps clarify the shortcomings of existing laws and direct future research. Although the performance criteria for steering laws can be broken down into more descriptive subcategories,[10] in general, an ideal steering law must

1) Accommodate singularities

2) Provide error-free torque to the precision of the hardware

3) Accommodate hardware limitations (such as gimbal-rate saturation and computational throughput)

4) Provide efficient performance (such as maximal usage of the available momentum space)

5) Require no knowledge of future torque commands

6) Be general enough to support the full range of maneuvers and CMG configurations (e.g. CMG failure cases)

Any CMG based attitude-control system must be implemented with the array's singularities in mind. Steering laws that prevent the CMGs from encountering singularities at all are broadly referred to as singularity-avoidance laws, whereas those that are designed to enable the array to pass through singularities are called singularity-robust laws. Steering laws that do not address singularities, such as the Moore-Penrose pseudoinverse, are generally inappropriate unless the attitude-control design restricts the array's workspace to a nonsingular region.[21] Instead of being used directly, such laws may be part of a more subtle scheme that does handle singularities.

Accuracy is an important performance metric for steering laws because CMGs are

Table 4 Summary of General Steering Law Characteristics.

Steering Law	Singularity Avoidance Method	Induced Torque Error	Gimbal Saturation Possible	Full Momentum Workspace Used	Instantaneous	Generalized for All Array Configurations
Ideal Steering Law	**Unknown**	**No**	**No**	**Yes**	**Yes**	**Yes**
Moore-Penrose Pseudoinverse	None	No	Yes	Yes	Yes	Yes
Singularity Robust Inverse w/ Torque Error	Inexact mapping of command to output torque	Large near singularity, small otherwise	Yes	Yes	Yes	Yes
Offline Planning	Path planning and/or optimization	No	No	Yes	No	Yes
Preferred Gimbal Angle	Initial gimbal angles keep array non-singular for specific torque commands	No	Yes	No	Yes, if properly initialized	No
Gradient/Null Motion	CMG null motion in non-singular direction	No	Yes	Yes, but has finite gimbal rates only if no impassable singularities present	Yes	No
Constrained	Operating in non-singular gimbal-angle subspace	None within workspace, but limited workspace	Dependent on array configuration	Dependent on array configuration	Yes	No

particularly well suited to highly agile spacecraft, such as commercial imaging satellites. Therefore the applications for which most CMG arrays are being considered have demanding requirements for precise attitude control. A large category of CMG steering laws--the Singularity Robust variety--intentionally adds error to the solution as a way to sidestep singularities, producing torque errors that are relatively small except when the array is nearly singular. While this method is easily implemented and can produce usable torque, that torque is precise enough and nonsingular only within a small sub-region of the available momentum. If the array approaches singularity, gimbal rates can exceed the hardware limits; accuracy is sacrificed, and the determinacy of the solution is not guaranteed. Accuracy requirements for agile spacecraft make exactness the driver instead of the mere simplicity of such laws.

CMG steering laws should also be designed to prevent infeasible commands to the hardware. In particular, an ideal steering law should never call for excessive gimbal rates or accelerations. Some categories of steering laws can produce gimbal rate saturation, resulting in reduced controllability. While these laws can provide some measure of singularity avoidance, an ideal solution necessitates that they do so without requiring gimbal saturation.

Any successful steering law must be shown to provide torque and momentum performance appropriate for the size, weight, and power of the array. The efficiency of different classes of steering laws is a metric that is open to debate, but it is generally agreed that methods that severely constrain the operating envelope of the array by design, particularly in CMG failure cases, are not ideal. Some types of steering laws fall into this category by sacrificing momentum workspace to handle singularities

(including some constrained laws such as scissored pairs of CMGs). However, an ideal law would maximize the use of the array's total momentum envelope while limiting the number of individual CMGs and the power used.

A steering law must also be capable of interpreting a torque command and implementing it in real time on the spacecraft with no explicit knowledge of the future. This requirement on array steering is distinct from any feedforward that the attitude-control might implement. Instantaneous responsiveness is ideal because laws that can manage it can directly map commands into CMG motion without the imprecision that comes with unavoidably imperfect future knowledge. Off-line approaches to developing singularity-free paths for the CMG array,[22] while often providing excellent simulated performance (if the algorithm is properly formulated and not overconstrained), generally require computationally intensive models that may be impractical on actual spacecraft hardware. Furthermore, these approaches cannot account for all of the subtleties, such as noise and unmodeled dynamics, which are inevitably present in any closed-loop system. Thus, it is desirable for an ideal steering law to be instantaneously responsive.

Finally, steering laws should be independent of the particular maneuvers commanded by the spacecraft and should not need to be replaced with an entirely different algorithm in the case of a CMG failure. The more general the steering law is with respect to the maneuver and the array geometry, the more robust the system is to unexpected torque commands or failure cases. Unfortunately, a generalized steering law is much more complicated to design, and thus many steering laws specify applicable array geometries[9,19,20]. While these solutions are often very well-suited to

their specific array geometry, an ideal steering law would be general enough to handle changes in the array configuration.

While Table 1 by no means offers as detailed or as nuanced a description as these different techniques deserve, it does provide a clearer picture of which steering laws are more promising. Some of the categories are intrinsically non-ideal by the proposed metrics. For example, offline planning approaches are by definition not instantaneous. So, it follows that the ideal solution to CMG steering is probably not to be found among these categories. However, working to understand some of the other laws in a more general way may provide the framework necessary for developing an ideal steering law. Algorithms that use constraints to steer the array on a non-singular path falls into one such category.

The remainder of this paper examines a generalized formulation for steering laws based on linear constraints. These laws constrain the motion of the CMGs, taking into account torque and angular momentum limitations a priori, in order to prevent the array from encountering internal singularities. By studying a more general form of this class of steering laws, it is possible to gain insight on better ways of designing them. While this paper focuses on linear constraints in particular, constraints need not always be linear with respect to the gimbal rates, as found by Kurokawa[8,23]. However, the linear formulation provides distinct advantages in implementation, making them worthy of in-depth study. Section III describes a general form for these steering laws and describes special cases of this form. Section IV presents simulation results for a new linearly-constrained steering law designed for Cornell's Violet nanosatellite, an in-orbit CMG testbed.

Generalized Form for Linearly-Constrained Steering Laws

A. Description

An expression for the commanded torques in terms of the gimbal rates is shown in Equation 1:

$$\tau_C = J(\Phi)\dot{\Phi} \tag{1}$$

where J is the Jacobian for the CMG array (the partial derivative of its total momentum with respect to the gimbal angles), τ_c is the commanded torque vector in body coordinates, and ϕ is the n×1 array of gimbal rates meant to achieve that torque. This equation is solved using a pseudoinverse as shown in Equation 2:

$$\dot{\Phi}(\tau) = J(\Phi)^{+}\tau_C \tag{2}$$

Many pseudoinverses exist[24] and can be used to solve for the CMG gimbal rates. The singularity-robust pseudoinverse[11] is an example. However, CMG steering laws, including those considered in this work, begin with an approach that uses the Moore-Penrose pseudoinverse, shown in Equation 3:

$$\dot{\Phi}(\tau) = J(\Phi)^{T}\left(J(\Phi)J(\Phi)^{T}\right)^{-1}\tau_C \tag{3}$$

The $J(\Phi)J(\Phi)^{T}$ term can be rank deficient, and therefore non-invertible, which is the mathematical basis for array singularity. So, as the first step in ensuring that the inverse of the $J(\Phi)J(\Phi)^{T}$ term exists, constraint equations can be appended to the Jacobian. Equation 4 is a general description of a set of linear constraint equations:

$$D = C\dot{\Phi} \tag{4}$$

where D is an $m \times 1$ matrix, and C is an $m \times n$ matrix. Equation 1 can be augmented as follows:

$$\begin{bmatrix} \tau_C \\ D \end{bmatrix} = \begin{bmatrix} J(\Phi) \\ C \end{bmatrix} \dot{\Phi} = A\dot{\Phi} \tag{5}$$

which leads to an augmented system matrix A. A non-zero D and C provide a more general form of a steering law that is based on the Moore-Penrose pseudoinverse. Alternatively, one can argue that C and D are zero in Equation 3 and that the resulting solution simply minimizes the norm of the gimbal rates. Equation 6 shows the more general form of a linearly constrained steering law:

$$\dot{\Phi}(\tau) = A(\Phi)^T \left(A(\Phi) A(\Phi)^T \right)^{-1} \tau_C \tag{6}$$

Using the constraint matrices not only minimizes the norm but can also provide the singularity avoidance properties required of an effectual steering law. Using an augmented form of A that includes the system kinematics and the constraints on the system, can ensure full rank for the inverse and thus avoid singularities. This description of linearly constrained steering laws provides a first step toward generalizing this class of steering laws. Since an appropriate set of D and C matrices can produce a singularity-free motion, the selection of these values is not trivial. Subsequent sections offer some insight into this process.

B. Principles of Constraint Design

The generalized form of the constrained steering laws in Equation 6 can accommodate diverse arrays and numbers of constraints. While the constraints must be linear with respect to the gimbal rates, common types of constraints take this form. For example, a holonomic constraint that specifies the gimbal angles explicitly can be written in the following form:

$$\tilde{D} = \tilde{C} \cdot \Phi(\tau) \tag{7}$$

Differentiating this type of constraint, assuming that the constraint is a linear combination of the gimbal angles and thus the $\tilde{C}$ matrix is constant, puts it into the form of Equation 4:

$$\dot{\tilde{D}} = \tilde{C} \cdot \dot{\Phi}(\tau) = C\,\dot{\Phi}(\tau) = D \tag{8}$$

This approach requires the specification of the initial conditions. The scissored-pair steering law is an example of this type of constraint and is discussed in more depth in subsequent sections. In general, freedom from singularities requires specific initial conditions (akin to preferred gimbal angles) and carefully chosen constraints. If they are chosen correctly, the resulting CMG gimbal motion is thereby constrained to a singularity-free subspace of all possible gimbal-angle combinations.

In general, such a formulation also allows for an arbitrary number of constraints, as an array of CMGs may be capable of producing singularity-free motion with either an underconstrained or an overconstrained Jacobian. However, for simplicity, the examples in the remainder of this paper consider only fully constrained systems, where the number of constraints *m* must result in a square Jacobian. Thus, when

considered against the number of CMGs available, n, for a three-dimensional space, the total number of constraints is:

$$m = n - 3 \tag{9}$$

The result is a deterministic, one-to-one mapping of momentum to gimbal angles. Naturally, a healthy spacecraft has $n \geq 3$ CMGs; any additional constraints exploit the null space represented by four or more CMGs. For example, controlling a three-dimensional momentum space with four CMGs requires only one constraint. A fully constrained system produces a square A matrix, which in turn means that the pseudoinverse in Equation 6 can be replaced with a simple matrix inverse. It is also worth noting that in order for a constraint-based steering law to operate properly, the constraint must be fully enforced despite its numerical implementation. Therefore, some amount of low-bandwidth feedback may be required to avoid an accumulation of numerical error that increasingly violates the constraint.

Finally, Equation 5 suggests that in order for the A matrix to be non-singular, the constraint matrix C must contain rows that are linearly independent of the Jacobian J at any time. Constraint equations must therefore comprise a complementary subspace to the rows of the Jacobian and simultaneously ensure that the J partition remains rank 3.

C. Example: Scissored-Pair CMGs

The well-established, linearly constrained steering law known as a scissored-pair arrangement provides a convenient example demonstrating how known steering laws fit into the generalized framework.[7] In a scissored-pair configuration, two CMGs

with parallel gimbal axes are constrained such that their gimbal angles are equal in magnitude and opposite in direction ($\phi_1 = -\phi_2$). Alternatively, the angles can be constrained to be the same ($\phi_1 = \phi_2$), but with gimbal axes exactly opposite each other. This simple constraint can be enforced either in hardware (which offers some additional benefits),[25] or in software. The scissoring motion caused by this constraint produces an output torque along a fixed direction determined by the gimbal axes, as shown in Fig.1. Therefore, complete six degree-of-freedom control requires three scissored pairs, i.e. six individual CMGs. The arrangement shown in Fig. 2 is used for the purposes of this example.

Scissored-pair arrangements of CMGs are singularity free except at the saturation singularities, where the pair produces the maximum momentum of which it is capable. If unconstrained, each of the pairs of CMGs would offer a 2*h*-radius circular momentum envelope with a singularity at the origin. With the constraint, the pair operates within a reduced but nonsingular cube-shaped envelope 4*h* on a side. Because

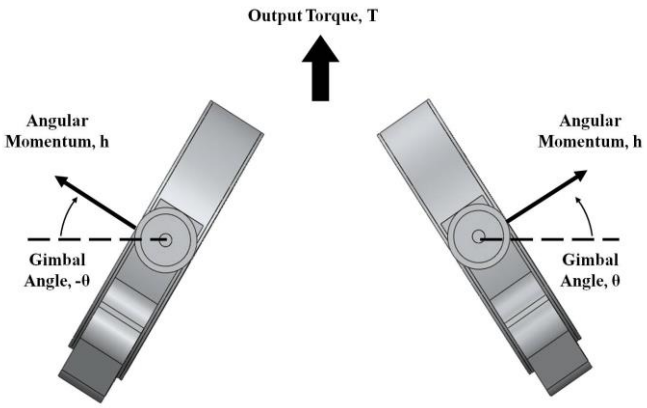

Fig. 1 Scissored Pair of CMGs.

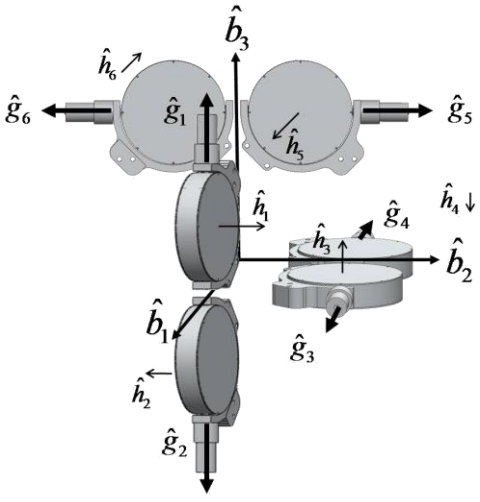

Fig. 2 Arrangement of Three Orthogonal Scissored Pairs.

saturation limit of the constrained system is well inside the overall array momentum boundaries, this configuration of CMGs is generally not considered cost-effective despite its singularity-avoidance properties and its relative simplicity.

Figure 2 shows six CMGs aligned along the three orthogonal axes in pairs with opposite gimbal axes. Whether or not a scissored-pair constraint is in force, its Jacobian is:

$$J = h\begin{bmatrix} -\cos\phi_1 & -\cos\phi_2 & 0 & 0 & -\sin\phi_5 & \sin\phi_6 \\ -\sin\phi_1 & \sin\phi_2 & -\cos\phi_3 & -\cos\phi_4 & 0 & 0 \\ 0 & 0 & -\sin\phi_3 & \sin\phi_4 & -\cos\phi_5 & -\cos\phi_6 \end{bmatrix} \tag{10}$$

For this arrangement to act as a collection of scissored pairs, the constraint equations can be expressed as the set of three equations:

$$\phi_1 - \phi_2 = 0;\ \phi_3 - \phi_4 = 0;\ \phi_5 - \phi_6 = 0 \tag{11}$$

Taking the derivative of these constraints as suggested in Equation 8 produces a similar constraint on the gimbal rates. In a matrix form, the gimbal-rate constraints are

$$\begin{bmatrix} 0 \\ 0 \\ 0 \end{bmatrix} = \begin{bmatrix} 1 & -1 & 0 & 0 & 0 & 0 \\ 0 & 0 & 1 & -1 & 0 & 0 \\ 0 & 0 & 0 & 0 & 1 & -1 \end{bmatrix} \dot{\Phi} \tag{12}$$

From Equation 5, the augmented linear equation is

$$\begin{bmatrix} \tau_1 \\ \tau_2 \\ \tau_3 \\ 0 \\ 0 \\ 0 \end{bmatrix} = \begin{bmatrix} -h\cos\phi_1 & -h\cos\phi_2 & 0 & 0 & -h\sin\phi_5 & h\sin\phi_6 \\ -h\sin\phi_1 & h\sin\phi_2 & -h\cos\phi_3 & -h\cos\phi_4 & 0 & 0 \\ 0 & 0 & -h\sin\phi_3 & h\sin\phi_4 & -h\cos\phi_5 & -h\cos\phi_6 \\ 1 & -1 & 0 & 0 & 0 & 0 \\ 0 & 0 & 1 & -1 & 0 & 0 \\ 0 & 0 & 0 & 0 & 1 & -1 \end{bmatrix} \dot{\Phi} = A_{SP}\,\dot{\Phi} \tag{13}$$

which defines A_{SP} as the scissored-pair A matrix. The required initial condition is that the gimbal angles for each pair begin with equal magnitude and opposite sign. The constraint enforces the requirement throughout subsequent motions. This fact allows one to simplify Equation13 and produce the determinant

$$\det\left(A_{SP}\right) = -8h^3\cos\left(\phi_1\right)\cos\left(\phi_3\right)\cos\left(\phi_5\right) \tag{14}$$

The singularity-avoidance properties of this particular steering law are evident in the determinant of the newly formed A_{SP} matrix from Equation 13. The singular points, i.e., where Equation 14 vanishes, are where ϕ_1, ϕ_3, and ϕ_5 become –π/2 or π/2 for each scissored pair. A_{SP} remains nonsingular at any point within this range. These angles represent the saturation of the gimbals, showing that the system has full rank for gimbal angles below saturation. While this result simply confirms what has already been known about scissored-pair steering laws, it serves as an example of the power of the generalized formulation.

Triplet Steering Law

The generalized form of the linear constrained steering law can also be used to better inform the development of new steering laws of this variety. The "triplet"

steering law was developed using the generalized framework and can be shown to yield effective singularity-free motion with the many advantages that constrained steering laws inherently possess.

A. Theoretical Discussion

The case of a planar CMG momentum envelope, where the gimbal axes of the CMGs are all parallel, provides a convenient starting point for the development of a steering law for sets of parallel CMGs. In such an array, a single CMG leads to a one-dimensional momentum manifold because only a single gimbal angle changes. With two CMGs, the momentum vectors can add to produce torque in both directions that span the plane, as long as the gimbal rates are kept within saturation limits. The mapping from a two-dimensional torque to two gimbal rates is one-to-one, which means that there is no alternative, singularity-free path that avoids those cases when the Jacobian is singular.

However, if three CMGs' momentum vectors lie in this plane (a "triplet"), the additional CMG adds a degree of freedom (so that, for example, an infinite number of gimbal angles relative to the body axes can correspond to the zero momentum state, as shown in Fig. 3). The three-CMG configuration has an internal singularity in which the three momentum vectors are collinear and two momentum vectors exactly cancel out. Such an arrangement is shown in Fig. 4. The momentum of this triplet array can be represented by the vector sum of the three component momentum vectors--that is, by arranging the three vectors head to tail. In this momentum-space representation, the internal singularity manifold is a ring 1h in radius around the center of the axes.

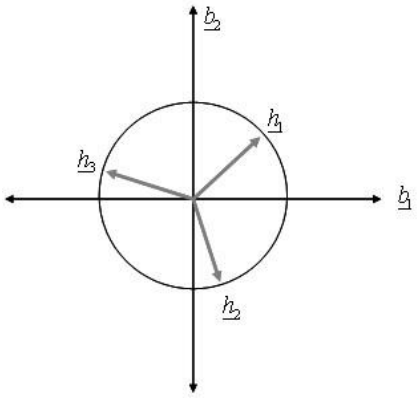

Fig. 3 Planar representation of CMG momentum in a zero-momentum state.

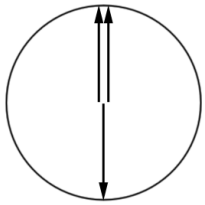

Fig. 4 Internal singularity for triplet arrangement.

Solving for the gimbal rates in a CMG triplet requires one constraint equation for a two-dimensional workspace. This constraint must be designed to successfully avoid the internal singularity while also providing the required torque by exploiting the null space of the Jacobian. The triplet configuration has a 2×3 Jacobian, as shown in Equation 15, where J_1 and J_2 are the top and bottom rows of the Jacobian, respectively.

$$J_{Planar} = \begin{bmatrix} -\sin\phi_1 & -\sin\phi_2 & -\sin\phi_3 \\ \cos\phi_1 & \cos\phi_2 & \cos\phi_3 \end{bmatrix} = \begin{bmatrix} J_1 \\ J_2 \end{bmatrix} \tag{15}$$

In order to ensure that the constraint equation maintains the rank of *J*, the constraint equation must be linearly independent of the two rows of the Jacobian at any instant and must keep those two rows independent of one another. If the cross-product of two vectors is non-zero, the two vectors are linearly independent. Therefore, a singularity-free constraint equation must include a scaled component in the direction of the cross-product of the two rows of the Jacobian. Equation 16 shows the constraints written in the form of Equation 4:[26]

$$D = d = \left[\beta_1 J_1 + \beta_2 J_2 + \beta_c \left(J_1 \times J_2 \right) \right] \dot{\Phi} = C \dot{\Phi} \tag{16}$$

where *d* is a scalar solution to the constraint equation, β_1 and β_2 are scaling values for the component of the vector in the direction of the Jacobian rows, and β_c is a non-zero scaling value for the constraint equation. The solution presented as an example uses a value of zero for β_1 and β_2 and a value of one for β_c, such that the constraint equation is as shown in Equation 17.

$$D = \left[J_1 \times J_2 \right] \dot{\Phi} = \left[\sin(\varphi_3 - \varphi_2) \quad \sin(\varphi_1 - \varphi_3) \quad \sin(\varphi_2 - \varphi_1) \right] \dot{\Phi} = C \dot{\Phi} \tag{17}$$

D determines the null motion needed to steer the array away from the internal singularity at 1*h*. Because *C* is orthogonal to the two rows of *J*, the singularities of the augmented matrix *A* (Equation 5) are simply the singularities of *J*.

B. Null-Space Constraint

Using the generalized constrained steering law formulation, the burden of

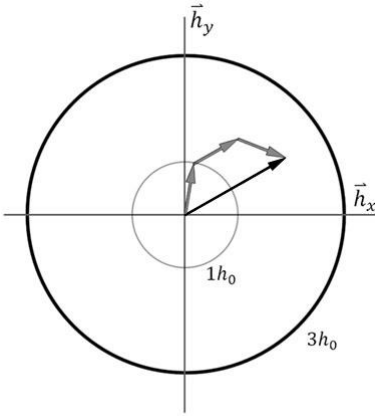

Fig. 5 Triplet CMGs in a trapezoid configuration.

designing the steering law shifts to designing a set of useful constraint equations. Within the context of a triplet CMG array, the theoretical guidelines for the constraint design make it possible to implement an efficient steering law that exploits the insights provided by the framework suggested by Equation 5.

One of the constraint designs that has proven to be exceptionally effective uses null-space commands to keep the CMGs in a "trapezoid" configuration in momentum space.[27] As shown in Fig. 5, one of the CMG momentum vectors in the trapezoid configuration is kept parallel to the array momentum vector, while the other two CMG momentum vectors form the sides of a trapezoid. All three vectors are parallel only at the edge of the momentum envelope. At the internal singularity at 1h the two vectors forming the sides are orthogonal to the vector parallel to the total momentum vector—an ideal configuration for traversing the singularity.

For any total momentum vector within the array's momentum envelope, there are six sets of gimbal angles that cause the momentum vectors to form a trapezoid such that they sum to the same total momentum vector. Some may be redundant. The proposed steering law first determines which of the six trapezoid configurations is closest to the current (non-trapezoidal) gimbal angle configuration. The "closest" configuration is the one that requires the least amount of null motion to move between it and the current configuration and is therefore the desirable target for the gimbal angles.[27] In implementation, this step is accomplished by computing the six possible trapezoidal sets of gimbal angles, and then comparing those six possibilities to the current set of gimbal angles. The trapezoidal gimbal angle set that is the closest in the 2-norm sense is then selected as the target configuration.[27]

The angles for the target trapezoid configuration are used in Equation 18 to solve for *D*:

$$D = \begin{bmatrix} \sin(\varphi_3 - \varphi_2) & \sin(\varphi_1 - \varphi_3) & \sin(\varphi_2 - \varphi_1) \end{bmatrix} K \left(\begin{bmatrix} \varphi_{1t} \\ \varphi_{2t} \\ \varphi_{3t} \end{bmatrix} - \begin{bmatrix} \varphi_1 \\ \varphi_2 \\ \varphi_3 \end{bmatrix} \right) \tag{18}$$

where φ_{nt} is the target gimbal angle for the nth CMG, and *K* is a 3×3 diagonal matrix of gains. The values of the entries of *K* determine how much effort is used to drive the CMGs to their closest trapezoid configuration and are chosen such that as much null-space effort as possible is used to keep the array close to a trapezoid without exceeding gimbal limits. The selection of entries in *K* can be done with brief numerical iteration or an optimization function.[27] For the simulations presented in this paper, the *K* values were chosen using a numerical optimization routine that searches through a grid of possible *K* matrices. All of these values are used to evaluate Equation 18 to produce a set of possible *D* values. These *D* values are then used in Equation 5 to solve for a set of $\dot{\phi}$ values that correspond to every potential *K* matrix. Values that would cause the gimbal rate or acceleration limits to be exceeded are discarded. From the remaining pool of *K* values, which now all meet the hardware limitations of the system, the *K* matrix that moves the array closest towards the desired trapezoid configuration in the next time step is selected. The resulting optimal *K* matrix cannot cause the system to exceed hardware limitations because it was explicitly selected to meet these constraints. Once the optimal values of the *K* matrix found, the corresponding gimbal rates are then sent to the actuators.

When implemented, this algorithm is not used close to the zero-momentum state because at zero momentum, there are infinitely many possible trapezoids instead of the usual six configurations. While torque is still available in any direction, the algorithm must be given a way of deciding the appropriate configuration of the momentum vectors without rapidly switching back and forth between two different target trapezoids. The constraint is therefore modified such that within a small radius of the zero momentum state, a Moore-Penrose pseudoinverse rule is used instead. Since the radius in which the pseudoinverse rule is used is much smaller than 1h, no problems with singularities are encountered by using the pseudoinverse, and the issue of very large gimbal rates near zero momentum is avoided. In the implementation on Cornell's Violet nanosatellite, the pseudoinverse rule is used only within 0.1h, which allows for enough null motion between 0.1h and 1h to properly condition the array. In the general case, the radius should be as small as possible but still large enough that the momentum can traverse the origin with bounded gimbal rates. In general, the choice of this radius depends on the application-specific requirement on simultaneously available torque and momentum.

C. Expansion to Three-Dimensional Momentum Values

While one CMG triplet spans only two degrees of freedom, it is straightforward to expand this steering law to all three attitude degrees of freedom. Two sets of triplets (six CMGs) are positioned such that the two planes are not parallel—i.e., gimbal axes are offset relative to one another and can be used together to exert torque in three directions. The angle between the planes determines the array's capability in spacecraft axes; so, it would likely follow from agility requirements and

the spacecraft's own inertia tensor. If the triplets are nonsingular, this configuration results in complete singularity-free control over two planes at an angle to one another and therefore spans the three-dimensional range of momentum values. In the example considered here, the triplets' gimbal axes are orthogonal to one another, as shown in Fig. 6. A three-axis triplet steering law requires two constraint equations, as described in Equation 19.

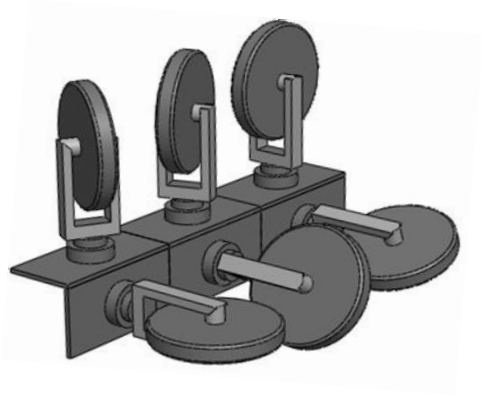

Fig. 6 Two Triplets of CMGs at Right Angles.

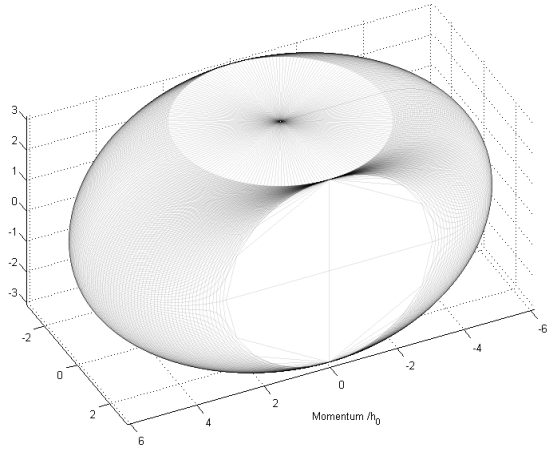

Fig. 7 Momentum envelope for two orthogonal triplets.

$$\begin{bmatrix} \tau_x \\ \tau_y \\ \tau_z \\ D_1 \\ D_2 \end{bmatrix} = \begin{bmatrix} 1 & 0 & 0 & 1 & 0 & 0 \\ 0 & 1 & 0 & 0 & 0 & 0 \\ 0 & 0 & 0 & 0 & 1 & 0 \\ 0 & 0 & 1 & 0 & 0 & 0 \\ 0 & 0 & 0 & 0 & 0 & 1 \end{bmatrix} \begin{bmatrix} \tau_{x_1} \\ \tau_y \\ D_1 \\ \tau_{x_2} \\ \tau_z \\ D_2 \end{bmatrix} = \begin{bmatrix} 1 & 0 & 0 & 1 & 0 & 0 \\ 0 & 1 & 0 & 0 & 0 & 0 \\ 0 & 0 & 0 & 0 & 1 & 0 \\ 0 & 0 & 1 & 0 & 0 & 0 \\ 0 & 0 & 0 & 0 & 0 & 1 \end{bmatrix} \begin{bmatrix} J_{1\,2\times3} & 0_{2\times3} \\ C_{1\,1\times3} & 0_{1\times3} \\ 0_{2\times3} & J_{2\,2\times3} \\ 0_{1\times3} & C_{2\,1\times3} \end{bmatrix} \begin{bmatrix} \dot{\varphi}_1 \\ \dot{\varphi}_2 \\ \dot{\varphi}_3 \\ \dot{\varphi}_4 \\ \dot{\varphi}_5 \\ \dot{\varphi}_6 \end{bmatrix} \quad (19)$$

where J_1 represents the 2×3 Jacobian of the first CMG triplet and J_2 the 2×3 Jacobian of the second triplet. C_1 and C_2 are the 1×3 constraint equations, as described in Equation 17, and D_1 and D_2 are solved for as described in Equation 18. The requested torque in the shared x-direction needs to be distributed to both CMG arrays, such that the sum of τ_{x_1} and τ_{x_2} in Equation 19 equals the requested torque in the x-direction. The transformation matrix in Equation 19 is determined by the orientation of the two triplets. In this case, the gimbal axes are pointed in the *y* and *z* directions such that the momentum envelope is greater in the *x* direction. The momentum envelope for this configuration is shown in Fig. 7. The maximum extent is 6*h* in the direction orthogonal to both gimbal axes and 3*h* in the other two directions.

D. Orthogonal Triplet Steering Simulation Results

The orthogonal-triplet steering law must be tested in both simulated and hardware environments in order to be considered a viable candidate for steering arrays for other spacecraft missions. This steering law is ultimately intended to be tested onboard Violet, Cornell University's entry into the University Nanosat-6 competition. Violet will be the first-ever high-agility nanosatellite, with up to 10 deg/s, 10 deg/s^2 and 60 deg/s^3 agility. In this role, it will serve as an experimental testbed for validating CMG

Table 5 Summary of Simulation Parameters.

Momentum per CMG
h = 0.31 Nms
Maximum CMG gimbal rate
$\dot{\varphi}_{\max}$ = 1.6 rad/s
Maximum CMG gimbal acceleration
$\ddot{\varphi}_{\max}$ = 9.6 rad/s^2
Inertia matrix (in satellite body axes)
$I_{body} = \begin{bmatrix} 2.001 & 0.116 & -0.010 \\ 0.116 & 2.017 & -0.009 \\ -0.010 & -0.009 & 2.161 \end{bmatrix}$
Gimbal axes for CMGs 1-6 (in satellite body axes)
$\hat{g}_1 = \begin{bmatrix} 0 \\ -\sqrt{2}/2 \\ -\sqrt{2}/2 \end{bmatrix}, \hat{g}_2 = \begin{bmatrix} 0 \\ \sqrt{2}/2 \\ \sqrt{2}/2 \end{bmatrix}, \hat{g}_3 = \begin{bmatrix} 0 \\ -\sqrt{2}/2 \\ -\sqrt{2}/2 \end{bmatrix}$ $\hat{g}_4 = \begin{bmatrix} 0 \\ \sqrt{2}/2 \\ -\sqrt{2}/2 \end{bmatrix}, \hat{g}_5 = \begin{bmatrix} 0 \\ -\sqrt{2}/2 \\ \sqrt{2}/2 \end{bmatrix}, \hat{g}_6 = \begin{bmatrix} 0 \\ -\sqrt{2}/2 \\ \sqrt{2}/2 \end{bmatrix}$

steering laws in orbit. Violet carries eight CMGs of which six can be used simultaneously, offering many possible array geometries, such as a pair of orthogonal triplets. Because the orthogonal-triplet steering law will be tested on Violet's hardware, the simulation testing environment uses parameters from Violet's CMG array, listed in Table 2.[28] The inclusion of the gimbal acceleration limit is especially important because this steering law will be implemented on actual flight hardware which cannot produce infinite gimbal accelerations.

In order to demonstrate the proposed steering law and thus the efficacy of the generalized formulation for linearly-constrained laws, the results of 510 rest-to-rest slew simulations are shown in Fig. 8, Fig. 9, and Table 3. The slews are randomized rotations between 30 and 180 degrees (which covers the interesting cases where the slews either cross or come close to the singularity) and are about randomized eigenaxes. The slews are shaped through an algorithm that ensures continuous derivatives at both ends of the slew. The final attitude of the spacecraft in each slew is properly randomized in order to ensure a uniform distribution.[29] Violet's kinematic limits are used to generate the slew, and Violet's hardware constraints taken into account in the steering law. Similar rest-to-rest slews exemplifying the capabilities of a six-CMG array will be completed in orbit.

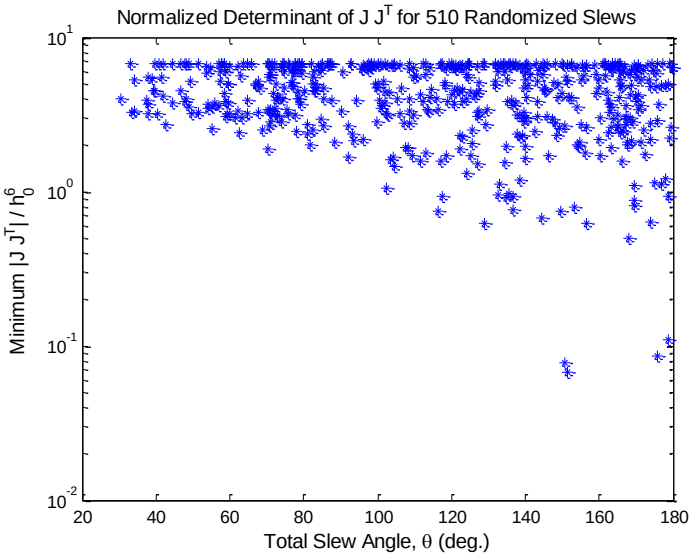

Fig. 8 Log minimum determinant of the normalized $J(\Phi)J(\Phi)^T$ vs. total slew angle.

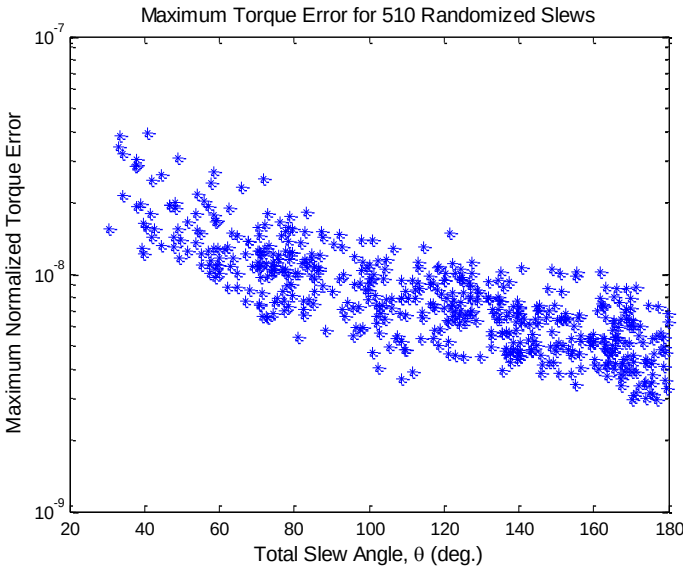

Fig. 9 Log maximum torque normalized error vs. total slew angle.

The minimum determinant of $J(\Phi)J(\Phi)^T$ is plotted as a function of the total slew angle in Fig. 8 on a semi-log plot in the y-axis. The determinant in the plot has been normalized by dividing out a factor of h^6 (which has a value of 8.875×10^{-4} in this simulation given Violet's h of 0.31 Nms) since $J(\Phi)$ is scaled by h. It is clear that the minimum determinant values do not reach the singularity value of zero over these 510 runs, providing confidence that the steering law is providing sufficient singularity avoidance. This result is supported by Fig. 9, which indicates a very low (10^{-8} Nm) normalized torque error over the randomized slews. Although this method produces exact solutions to the commanded torque, the system still has small errors associated with the array's inability to immediately match the magnitude of the demanded torque. These errors are the direct result of the imposed constraints on the available gimbal accelerations. The values in this plot were normalized by dividing out the factor of six times the maximum CMG torque (2.976 Nm for Violet).

Additional statistics on the Monte Carlo results are published in Table 3. The different values for an individual slew are listed down the first column and the statistical value for each is given in the appropriate row. The maximum values for the gimbal rate and acceleration never exceed the hardware limitations described in Table 2. The very low torque error is also evident in these statistics.

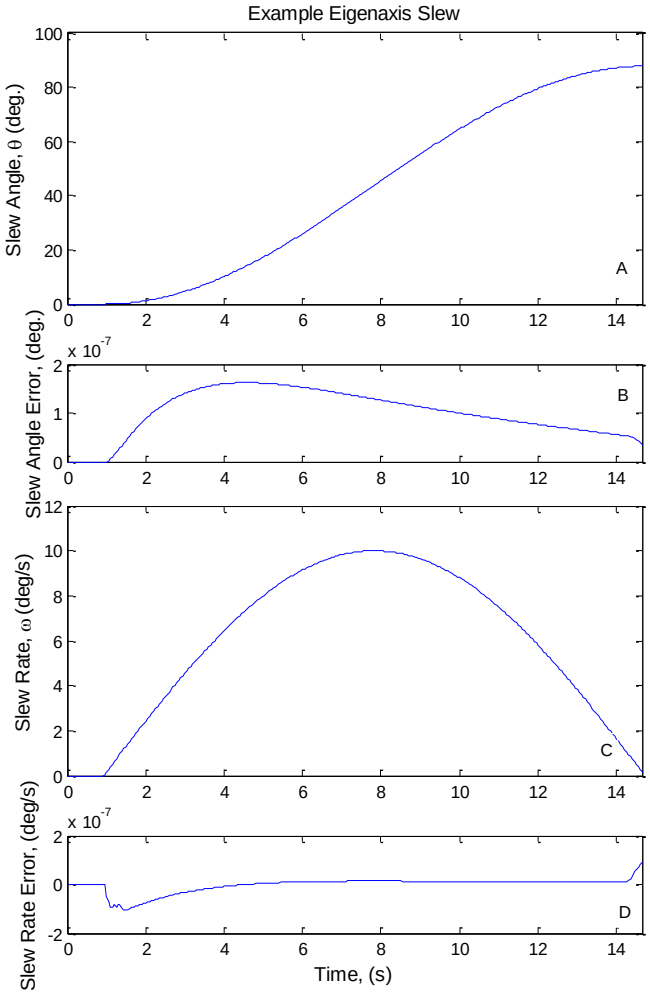

Fig. 10 Example slew rotation angle, angle tracking error, angular rate, and rate error.

To provide more detailed descriptions of the steering law's effect on a slew, results for a randomly selected example slew are shown in Fig. 10 and Fig. 11. Figure 10 shows the rotation angle and angular velocity and their errors with respect to the target slew. As is evident in the plots, both errors remain small throughout the sample maneuver. Figure 11 shows the torque applied by the CMGs, the error with respect to

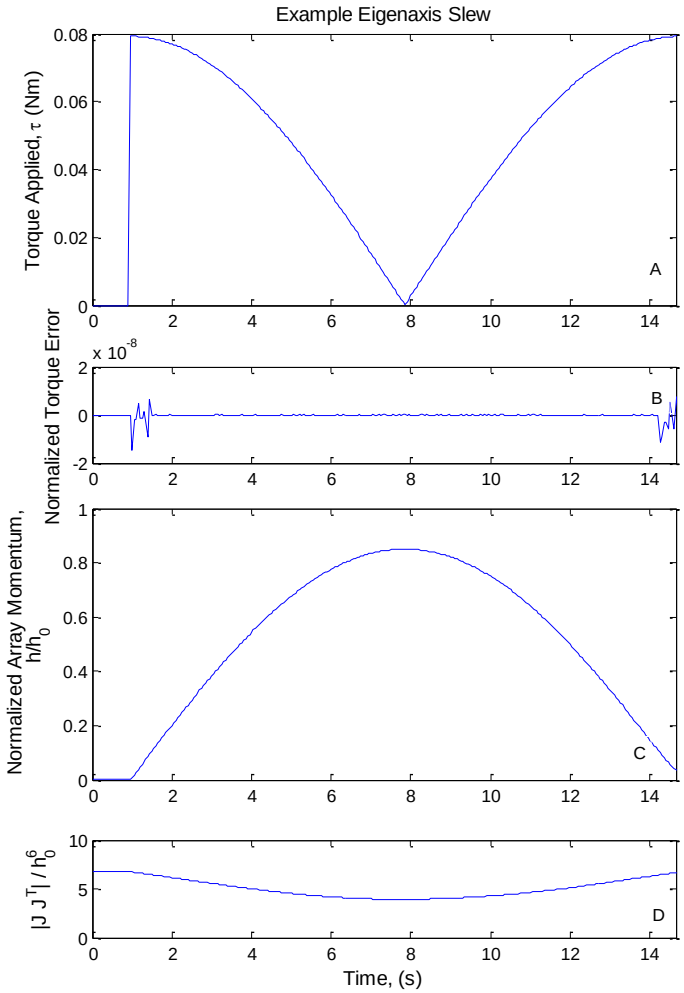

Fig. 11 Example slew torque applied (by CMG array on spacecraft), torque error normalized by 6x the max CMG torque, array momentum normalized by h, and determinant of $J(\Phi)J(\Phi)^T$ normalized by h^6

the torque requested by the spacecraft, the magnitude of the angular momentum of the CMG array, and the determinant of $J(\Phi)J(\Phi)^T$. The array is able to provide the requested torque with very low error, even when the array is near the region where singularities are possible ($1h$). While a decrease in the determinant of $J(\Phi)J(\Phi)^T$ is noticeable, it is still far from zero, especially when the h^6 scaling is taken into account. The motion of the CMGs throughout the example maneuver can be seen in Fig. 12, with a detail of the gimbal rates included for clarity in Fig. 13. The gimbal rates and accelerations remain within their hardware constraints for the entirety of the slew, which contributes to the low torque error since the commanded CMG motion is physically realizable.

Table 6 Summary of Monte Carlo Results.

Value Per Slew: / Over All MC Runs:	**Min.**	**Max.**	**Mean**	**Standard Deviation**
Maximum Gimbal Rate (rad/s) $\dot{\varphi}_{\max}$	0.0551	0.4680	0.2388	0.0750
Maximum Gimbal Acceleration (rad/s²) $\ddot{\varphi}_{\max}$	0.9254	9.3092	5.2164	1.8835
Maximum Torque Error (Nm) τ_{error}	0.087e-7	1.161e-7	0.265e-7	0.153e-7
Maximum Momentum of the Array (Nms) h	0.5572	1.2066	0.9085	0.1715

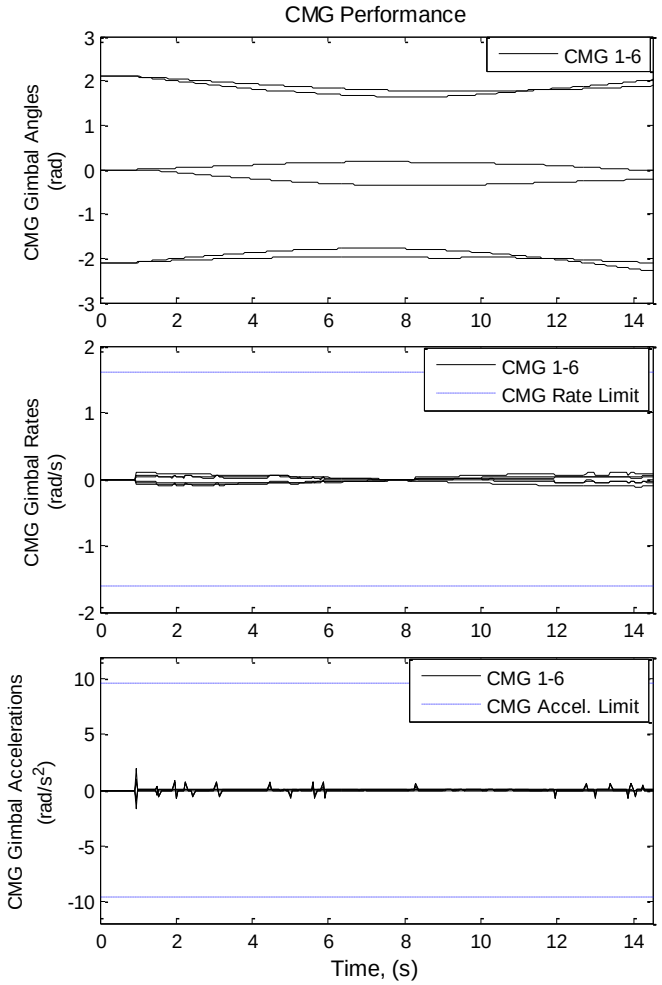

Fig. 12 Example slew CMG gimbal angles, rates and accelerations, as well as the limitations associated with the constraints of the hardware.

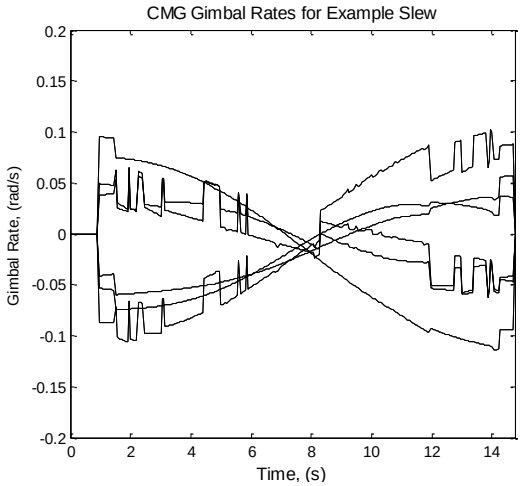

Fig. 13 Detailed plot of the gimbal rates.

Conclusions

A constrained steering law provides an error-free, instantaneous algorithm for applying attitude-control torques with control moment gryo (CMG) arrays while avoiding singularities. The general framework proposed here for describing the steering laws with constraint equations that are linear with respect to the gimbal rates suggests that by choosing linear constraints that lie in a subspace orthogonal to the CMG Jacobian, an augmented system Jacobian A can be made singularity free. This fact is demonstrated with a simple scissored-pair array example. Taking this idea one step further, one can define two-dimensional singularity-free momentum envelopes with a triplet set of CMGs. These triplets use a constraint that is orthogonal to the rows of the system Jacobian. It is possible to obtain momentum in all three attitude degrees of freedom by using two sets of CMG triplets arranged in non-parallel planes with a steering law responsible for distributing the torque between the two singularity-free triplets.

An example of such a steering law is demonstrated through a simulation that shows its singularity avoidance properties. A Monte Carlo simulation using randomized slews shows that the example steering law performance is not slew-dependent. Although this steering law is triplet-specific and neither requires a minimal number of CMGs nor is general to a variety of CMG arrays, this example demonstrates the power of the generalized framework for developing singularity free steering laws. Further work should investigate the possibility of using non-holonomic constraints in the context of the generalized formulation, and extensions of this work should attempt to describe a generalized formulation for all constraint-based methods, even those that

are nonlinear in the gimbal rates. Once such an algorithm is developed, a study of various CMG configurations can be performed to determine which geometries provide the best balance of cost-effectiveness and technological feasibility.

Acknowledgments

L. Jones thanks the NDSEG for providing the funding for this work and Dan Brown and Michele Carpenter for their advice and assistance. R. Zeledon wishes to thank NACME and the Alfred P. Sloan Foundation for providing support for this work.

References

[1] Schaub, H., and Junkins, J. "Singularity Avoidances Using Null Motion and Variable Speed Control Moment Gyros" *Journal of Guidance Navigation and Control*, Vol. 23, No. 1, Jan.-Feb. 2000, pp. 11-16.

[2] Ahmed, J. and Bernstein, D. "Adaptive Control of Double-gimbal Control-Moment Gyro with Unbalanced Rotor" *Journal of Guidance, Control, and Dynamics*, Vol. 25, No. 1, Jan.-Feb. 2002, pp. 105-115.

[3] Oh, H., and Vadali, S. "Feedback Control and Steering Laws for Spacecraft Using Single Gimbal Control Moment Gyros" *Journal of the Astronautical Sciences*, Vol 39, No. 2, April-June 1991, pp. 183-203.

[4] Hamilton, B. Underhill, B. "Modern Momentum Systems for Spacecraft Attitude Control" *29th AAS Guidance and Control Conference,* Breckenridge, CO, Feb4-8, 2006.

[5] Paradiso, J. A., "Global Steering of Single Gimballed Control Moment Gyroscopes Using a Directed Search," *Journal of Guidance, Control, and Dynamics*, Vol. 15, No. 6, 1992, pp. 1236–1244.

[6] M. Peck, B. Hamilton, and B. Underhill, "Method and System for Optimizing Torque in a CMG Array," U.S. Patent 7014150, March 21, 2006.

[7] Cunningham D. and Driskill, G. “A Torque Balance Control Moment Gyroscope Assembly for Astronaut Maneuvering” NASA 19720018745, 1972

[8] Kurokawa, H. “Constrained Steering Law of Pyramid-Type Control Moment Gyros and Ground Tests” *Journal of Guidance, Control, and Dynamics*, Vol 20, No. 3, May-June 1997, pp. 445-449.

[9] Kurokawa, H. “Survey of Theory and Steering Laws of Single-Gimbal Control Moment Gyros” *Journal of Guidance, Control, and Dynamics*, Vol. 30, No. 5, Sept.-Oct. 2007, pp. 1331-1340.

[10] NASA Marshall Space Flight Center. *A Comparison of CMG steering laws for high energy astronomy observatories (HEAOs),* NASA TM X-64727, 1972.

[11] HBedrossian, N.H, Paradiso, J., HBergmann, E.H, HRowell, D.H, “Steering Law Design for Redundant Single-Gimbal Control Moment Gyroscopes,” *AIAA Journal of Guidance, Control, and Dynamics,* Vol. 3, No. 6, Nov.-Dec. 1990, pp. 1083-1089.

[12] Wie, B., Bailey. D., Heiberg. C. "Singularity Robust Steering Logic for Redundant Single-Gimbal Control Moment Gyros," *Journal of Guidance, Control, and Dynamics*, Vol. 24, No. 5, pp 865-872.

[13] Cornick, D.“Singularity Avoidance Control Laws for Single Gimbal Control Moment Gyros” *Guidance and Control Conference*, Boulder, NASA TM X- 64790, 1979.

[14] Ford, K. and Hall, C., “Singular Direction Avoidance Steering for Control-Moment Gyros” *Journal of Guidance, Control and Dynamics,* Vol. 23, No. 4, July – Aug. 2000, pp 648 – 656.

[15] Wie, B., “New Singularity Escape/Avoidance Steering Logic for Control Moment Gyro Systems,” *Proceedings of the AIAA Guidance, Navigation, and Control Conference,* Austin, TX, 2003.

[16] Paradiso, J.“Global Steering of Single Gimballed Control Moment Gyroscopes Using a Directed Search” *Journal of Guidance, Control, and Dynamics,* Vol. 15, No. 5, 1992, pp. 1236-1244.

[17] Vadali, S. R., Oh, H. S., and Walker, S. R., "Preferred Gimbal Angles for Single Gimbal Control Moment Gyros," Journal of Guidance, Control and Dynamics, Vol. 13, No. 6, 1990, pp. 1090-1095.

[18] Hefner, R., and McKenzie, C., "A Technique for Maximizing the Torque Capability of Control Moment Gyro Systems," *Astrodynamics*, Vol. 54, No. AAS 83-387, 1983, pp. 905–920.

[19] Yoshikawa, T."Steering Law for Roof Type Configuration Control Moment Gyro System" *Automatica*, Vol. 13, 1979, pp. 359 -368.

[20] M. R. Elgersma, D. P. Johnson, M. A. Peck, B. K. Underhill, G. Stein, B. G. Morton, and B. J. Hamilton, "Method and system for controlling sets of collinear control moment gyroscopes," U.S. Patent 20070124032, Nov. 30, 2005.

[21] Farmer, J."A Reactive Torque Control Law for Gyroscopically Controlled Space Vehicles" NASA TM X- 64790, 1973.

[22] Fleming, A., and Ross, M., "Singularity-Free Optimal Steering of Control Moment Gyros," *Proceedings of the AAS/AIAA Astrodynamics Conference*, Tahoe, CA, vol. 123, No. 3, 2006, pp. 2681-2700.

[23] Kurokawa, H. "Exact Singularity Avoidance Control of the Pyramid Type CMG System" *Proceedings of the AIAA Guidance, Navigation, and Control Conference*, Washington D.C., 1994, pp. 170-180.

[24] Udwadia, F. and Kalaba, R. *Analytical Dynamics*. Cambridge University Press, 1996.

[25] Brown, D., and Peck, M., "Scissored-Pair Control Moment Gyros: A Mechanical Constraint Saves Power," *Journal of Guidance, Control, and Dynamics*, vol. 31, No. 6, pp. 1823-1826, 2008.

[26] Jones, L., and Peck, M., "A Generalized Framework for Linearly-Constrained Singularity-Free Control Moment Gyro Steering Laws," *AIAA Guidance, Navigation, and Control Conference*, Chicago, IL, Aug 10-13, 2009

[27] Zeledon, R. and Peck, M., "Singularity-Free Constrained Steering Law for Triplet Control Moment Gyros," *AIAA Guidance, Navigation, and Control Conference*, Toronto, ON, Aug 2-5, 2010.

[28] Gersh, J. and Peck, M., "Violet: A High-Agility Nanosatellite for Demonstrating Small Control-Moment Gyroscope Prototypes and Steering Laws" *AIAA Guidance, Navigation and Control Conference*, Chicago, IL, Aug 10-13, 2009.

[29] Peck, M., "Uncertainty Models for Physically Realizable Inertia Dyadics" *Journal of Astronautical Sciences*, Vol. 54, No. 1 2006